International Journal of Thermofluids 31 (2026) 101541

Contents lists available at ScienceDirect

International Journal of Thermofluids

journal homepage: www.elsevier.com/locate/ijtf

Modeling and simulation of radiative MHD nanofluid flow with Joule heating over a variable-thickness sheet

Mahmmoud M. Syam [a], Muhammed I. Syam [b],*, Kenan Yildirim [c]

[a] Mechanical and Industrial Engineering Department, Abu Dhabi University, P.O. Box 59911, Abu Dhabi, United Arab Emirates
[b] Department of Mathematical Sciences, UAE University, P.O. Box 15555, Al Ain, United Arab Emirates
[c] Mus Alparslan University, Mus, Turkey

ARTICLE INFO

Keywords:
Heat transfer
Electromagnetic heating
Nonlinear thermal boundary layer
Powell–Eyring fluid model
Variable-thickness surface
Radiative heat transport

ABSTRACT

This study investigates the unsteady squeezing flow and heat transfer characteristics of a graphene-oxide/water nanofluid confined between two parallel plates undergoing time-dependent motion. A similarity transformation is used to convert the governing nonlinear partial differential equations into a set of coupled boundary-value problems, which are then solved using a modified operational matrix method (OMM). The proposed formulation avoids the stiffness commonly encountered in traditional OMM by introducing a forward-based coefficient computation strategy, reducing computational effort while maintaining high accuracy. The numerical results are validated through L_2 truncation error, boundary-condition deviation analysis, and comparison of the local Nusselt number against reference solutions, showing an error on the order of 10^{-14}. A detailed parametric investigation is conducted to examine the influence of Brownian motion (Nb), thermophoresis (Nt), squeeze number (S), Eckert number (Ec), and Lewis number (Le) on velocity, temperature, and concentration distributions. The results show that increasing Nb by 0.1 leads to approximately a 6%–12% rise in peak temperature gradients, while higher Nt enhances thermal diffusion and reduces concentration gradients by nearly 8%–15% depending on ζ. The squeeze parameter accelerates the flow and increases the wall shear stress by about 10%, whereas Ec significantly boosts the thermal boundary layer due to viscous dissipation effects. Source terms associated with nanoparticle diffusion, viscous heating, and unsteady squeezing motion play a key role in shaping the overall transport behavior. Overall, the modified OMM offers a fast, stable, and highly accurate alternative for solving nonlinear nanofluid boundary-value problems, and the presented results provide deeper insight into the thermal and mass transport mechanisms of graphene-oxide nanofluids under unsteady squeezing motion.

1. Introduction

From an industrial and technological standpoint, the study of heat and mass transfer is not just a theoretical concept, but a crucial tool in a wide range of practical applications. These include polymer processing, glass fiber manufacturing, aerodynamic design, plastic film production, and the cooling and drying operations involved in paper, textile, dye, and lubricant industries. Understanding these principles is essential for professionals in fluid mechanics, chemical engineering, and related fields, as it directly impacts their work and the industries they serve. A comprehensive constitutive equation that can represent all characteristics of non-Newtonian fluids has yet to be established in the literature. Consequently, various models have been developed to describe the rheological behavior of these fluids, depending on their physical nature and material composition. Among these, the Powell–Eyring fluid model, with its ability to effectively model complex behaviors encountered in chemical and process engineering systems, has proven to be particularly significant. This model offers distinct advantages, such as physical realism, mathematical simplicity, and stability when compared to other non-Newtonian formulations. It characterizes shear-thinning behavior typical of substances like human blood, toothpaste, and ketchup. Numerous researchers have investigated the physical and thermal properties of Powell–Eyring fluids. For instance, Hayat et al. [1] examined the influence of variable thermal properties on Eyring fluid flow using the Cattaneo–Christov heat flux model as an alternative to Fourier's law to capture non-Fourier heat conduction effects, which refer to heat conduction that does not follow the traditional Fourier's law of heat conduction. Jalil et al. [2] employed a self-similar approach to obtain analytical solutions for parallel free-stream Powell–Eyring fluid flow. Akbar et al. [3] analyzed the influence of magnetic fields on the flow over a stretching surface, revealing that increasing magnetic intensity

* Corresponding author.
E-mail address: m.syam@uaeu.ac.ae (M.I. Syam).

https://doi.org/10.1016/j.ijft.2025.101541
Received 20 October 2025; Received in revised form 2 December 2025; Accepted 22 December 2025
Available online 31 December 2025

and the fluid parameter enhance resistance to motion. Furthermore, Hayat et al. [4] studied three-dimensional thermally radiative magnetohydrodynamic (MHD) Powell–Eyring flow, reporting that both surface friction and fluid–solid interaction intensify with higher values of the fluid parameter and Hartmann number. Rehman et al. [5] explored the flow characteristics within a vertical cylindrical geometry, while Qayyum et al. [6] investigated nonlinear convective MHD flow of Powell–Eyring nanofluids under Newtonian heating conditions, noting that the rate of heat transfer increases with the thermophoretic parameter. Finally, Khan et al. [7] utilized a parabolic approach to develop a solution framework for chemically reactive Powell–Eyring nanofluid flow problems. The efficient thermal management of microelectronic devices, a crucial aspect of modern technological systems, has seen a significant shift with the emergence of nanofluids. These innovative heat transfer media, comprising nanoscale solid particles suspended in conventional base fluids, have garnered substantial interest in recent years. Typically, these fluids are created by dispersing ultrafine nanoparticles into base liquids such as water, oil, or ethylene glycol through mechanical agitation or chemical stabilization methods. Nanofluids, with their exceptional thermophysical properties, have found diverse applications, from engine cooling to electronic device temperature regulation, biomedical processes, and the design of efficient heat exchangers, making them a versatile solution in the field of thermal management. Choi [8,9], a pioneer in the field, was among the first to introduce the concept of nanofluids. His work involved dispersing nanoparticles into a base fluid like water and demonstrating that these suspensions possess significantly higher thermal conductivities compared to the pure base fluids. Subsequent experimental investigations by Kang et al. [10] and Yoo et al. [11] confirmed that nanofluids enhance heat transfer efficiency due to their superior energy transport capabilities. Mahanthesh et al. [12] further extended this research by analyzing three-dimensional magnetohydrodynamic (MHD) flow of Powell–Eyring nanofluid over a stretching surface, incorporating the effects of Joule heating, thermal radiation, and viscous dissipation. Their findings indicated that temperature rises with increasing Brownian motion and thermophoretic parameters. Similarly, Ibrahim [13] conducted a comprehensive exploration of mixed convective stagnation-point flow of a viscous nanofluid subject to MHD and radiation effects, concluding that the radiation parameter intensifies the thermal boundary layer and temperature distribution. Abbas et al. [14] investigated nanofluid flow over a cylindrical surface under slip conditions, highlighting the influence of radiation and thermophoresis on the heat transfer rate. Moreover, Nadeem and Saleem [15] examined the flow behavior of Powell–Eyring fluid generated by a rotating cone, providing deeper insights into the complex rheological and thermal characteristics of such non-Newtonian nanofluids. Malik et al. [16] delved into the flow behavior of Eyring–Powell fluid over a stretchable cylindrical surface, taking into account temperature-dependent viscosity. Their analysis unveiled a significant finding: an increase in the Reynolds and Prandtl numbers leads to a substantial reduction in the thickness of the thermal boundary layer. Hussain et al. [17] undertook a study on the magnetohydrodynamic (MHD) flow of a Sisko nanofluid along a stretching cylinder, incorporating the effects of viscous dissipation and Joule heating. Their findings, a significant contribution to the field, demonstrated that both viscous dissipation and Joule heating notably elevate the temperature of the fluid. Similarly, Rashad et al. [18] examined the influence of Joule heating in the flow of a viscous nanofluid past a cylindrical surface with convective boundary conditions. They observed that this phenomenon considerably enhances heat transport within the fluid, a finding of great importance. Srinivasacharya et al. [19] explored a novel area of research, non-Darcy MHD flow over a vertically oriented porous plate, considering ion-slip and Hall current effects. Their findings, which revealed that increasing magnetic field strength augments skin friction while diminishing heat transfer rates, add a new dimension to the field. Shojaei et al. [20] studied second-grade fluid flow over a stretchable cylinder, incorporating Soret and Dufour effects, a unique approach. In contrast, Rehman et al. [21] analyzed the thermal behavior of Powell–Eyring MHD fluid over an inclined cylinder under the influence of Joule heating, noting a pronounced rise in temperature. Imtiaz et al. [22] investigated mixed convective Casson nanofluid flow past a stretchable cylinder with convective boundary conditions, and Babu et al. [23] analyzed convective MHD Jeffrey fluid flow generated by a stretching sheet, focusing on the effects of Joule heating. Kamran et al. [24] examined the MHD flow of a Casson nanofluid under slip and Joule heating conditions, reporting findings with practical implications: concentration increases with higher Prandtl number, thermophoretic parameter, and Casson fluid parameter, but decreases with greater Lewis number and Brownian motion parameter. Muhammad et al. [25] explored entropy generation and activation energy in Darcy–Forchheimer flow over a curved surface, extending the understanding of energy dissipation mechanisms in porous systems, which is crucial for practical applications. Additional works [26–28] have examined the integration of nanoparticles and fins within heat exchangers and porous media, highlighting how fin geometry and length influence thermal discharge performance. Sheikholeslami et al. investigated various nanoparticle shapes using a homogeneous nanofluid model, formulating the problem through partial differential equations solved via the Galerkin finite element method. Furthermore, refined models for porous media flows incorporating entropy analysis were proposed in Refs. [29,30]. Other investigations [31–33] focused on non-Newtonian fluid flows considering convective heat transfer, porous media, and thermal radiation effects. Khan et al. [34,35] provided comprehensive studies on non-Newtonian fluid behavior involving homogeneous and heterogeneous chemical reactions, second-order slip conditions, and entropy generation, offering more profound insight into the coupled transport mechanisms governing such complex flow systems. The present study is devoted to investigating the magnetohydrodynamic (MHD) flow characteristics of a Powell–Eyring nanofluid over a nonlinearly stretchable surface with variable thickness, incorporating the effects of viscous dissipation, thermal radiation, and Joule heating. A significant aspect of our methodology is the use of the operating matrix method, a powerful numerical approach, to analyze the variations in velocity, temperature, and concentration distributions.

The recent literature published between 2024 and 2025 shows a clear push toward more detailed modeling of magnetohydrodynamic and non-Newtonian nanofluid systems, with a particular emphasis on coupling multiple transport mechanisms such as viscous dissipation, Joule heating, and thermal radiation. Several works, including those by Mukhtar et al. and Sankari et al. demonstrate that modern nanofluid research increasingly integrates realistic effects such as dual stratification, porosity, and nonlinear stretching geometries to better replicate industrial and manufacturing conditions. These studies collectively confirm that contemporary MHD flow models are no longer limited to simplified Newtonian assumptions; instead, they involve multilayered physics where heat generation, magnetic fields, and complex rheology interact in ways that strongly influence thermal boundary-layer behavior. Similar trends appear in the studies of Mathews and Talla, Magdy and co-authors, and Adilakshmi et al. all of which show that boundary-layer flows over stretching surfaces continue to serve as versatile platforms for studying industrial processes ranging from polymer sheet fabrication to thermal coating technologies [36–39]. At the same time, recent analyses of hybrid nanofluids and entropy generation, such as those by Rafique and Mahmood or Ogboru and colleagues, highlight a growing interest in quantifying the energetic quality of these flows and their sensitivity to variable viscosity, temperature-dependent properties, and chemical reactions. These papers underline the need for models that accurately represent micro-scale transport mechanisms, particularly when heat sources, external magnetic fields, or high shear rates are present. Studies like those by Sharma and Jain further show that modern research increasingly incorporates slip conditions, variable thermal conductivities, and nonlinear diffusion, signaling a shift toward boundary-layer formulations that more accurately capture the

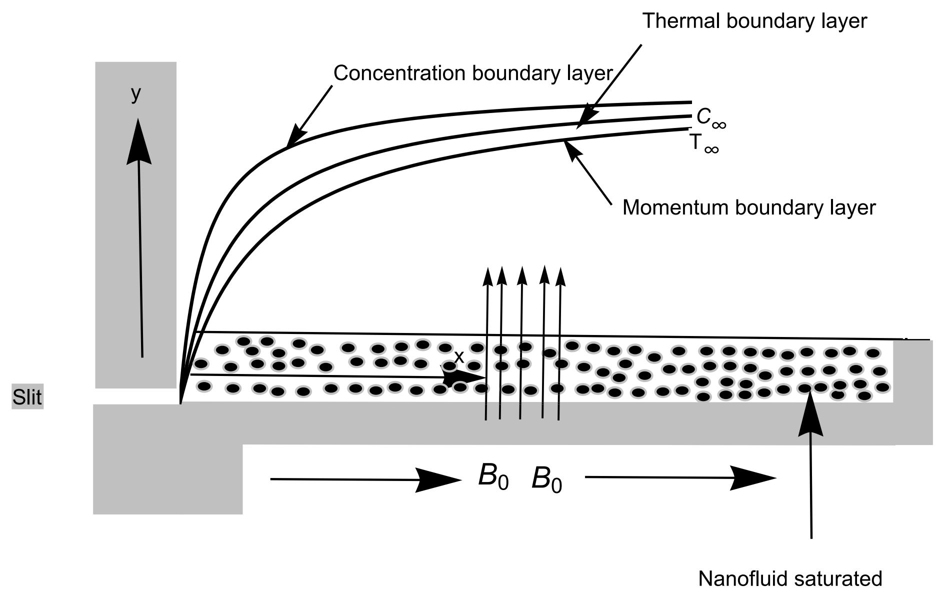

Fig. 1. Fluid flow dynamics of a nanoparticle suspension.

realities of high-performance cooling, material processing, and energy-conversion technologies. Together, these recent publications illustrate an evolving field where advanced rheological models and multiphysics couplings are central to predicting and optimizing nanofluid behavior, directly supporting the methodological and physical framework adopted in your article [40–43].

2. Mathematical formulation

In this study, a steady, two-dimensional, incompressible flow of a Powell–Eyring nanofluid over a nonlinear stretching surface of variable thickness is investigated. The coordinate system is chosen such that the x-axis lies along the surface in the direction of stretching and the y-axis is normal to it. The velocity components in these directions are denoted by u and v, respectively. The surface is stretched with a velocity $U_w(x) = U_0(x+a)^n$, where U_0 is reference velocity and a is a positive constant and n characterizes the degree of nonlinearity. The surface thickness is assumed to vary as $\delta(x) = \delta_0(x+a)^{\frac{1-n}{2}}$, where δ_0 is a reference thickness. We will assume that δ_0 is small so that the sheet surface is sufficiently thin. For the sake of clarity, we consider the plate described at

$$y = A(x+a)^{\frac{1-n}{2}}.$$

A magnetic field of strength B is applied in the direction normal to the plate surface. The geometry of the problem is illustrated in Fig. 1. The governing equations include the effects of viscous dissipation and nanoparticle diffusion. The governing equations, assumptions, and nondimensional parameters used in this study are grounded in well-established formulations for non-Newtonian boundary-layer flows and nanofluid transport. The momentum, energy, and concentration equations are derived directly from the conservation of mass, momentum, and energy for an incompressible Powell–Eyring fluid in the presence of magnetic fields, thermal radiation, and nanoparticle diffusion. The Powell–Eyring constitutive model is adopted due to its demonstrated capability to capture shear-thinning behavior common in many industrial and engineering fluids, and its suitability for boundary-layer analysis is supported by extensive prior research. The assumptions of steady laminar flow, thin boundary-layer approximation, and incompressibility are standard in stretched-surface flow problems and have been widely validated in theoretical and experimental studies on nanofluids and MHD flows. The nondimensional parameters introduced in the similarity transformations—such as the magnetic parameter H, Prandtl number Pr, Brownian motion parameter N_b, thermophoresis parameter N_t, Lewis number Le, radiation parameter R, and Eckert number Ec are classical dimensionless groups obtained through systematic scaling of the governing equations. Each parameter quantifies the relative strength of a specific physical mechanism, including momentum diffusion, thermal conduction, viscous dissipation, radiative heat transfer, and nanoparticle transport. The chosen parameter ranges are consistent with those reported for water-based nanofluids and magnetohydrodynamic boundary-layer flows, ensuring that the simulations remain physically realistic and the conclusions broadly applicable, [35]. Each term in the equations has the following physical interpretation:

- **Continuity equation**

$$\frac{\partial u}{\partial x} + \frac{\partial v}{\partial y} = 0. \tag{2.1}$$

This equation expresses the conservation of mass for an incompressible fluid. The first term $\partial u/\partial x$ accounts for the variation of velocity in the x-direction, while the second term $\partial v/\partial y$ represents the velocity variation normal to the surface. Their sum being zero ensures that the net volume flux in the control volume remains constant.

- **Momentum equation in the x–direction**

$$u\frac{\partial u}{\partial x} + v\frac{\partial u}{\partial y} = v\frac{\partial^2 u}{\partial y^2} + \frac{1}{\rho\beta_c}\frac{\partial^2 u}{\partial y^2} - \frac{1}{2\rho\beta c^3}\frac{\partial^2 u}{\partial y^2}\left(\frac{\partial u}{\partial y}\right)^2 - \frac{\sigma B^2 u}{\rho}. \tag{2.2}$$

The first two terms on the left-hand side represent convective acceleration in the streamwise and normal directions, respectively. The first term on the right-hand side denotes viscous diffusion, accounting for the internal friction of the fluid. The term $-(\sigma B_0^2/\rho)u$ represents the magnetic Lorentz force acting opposite to the motion, which resists the fluid flow. The additional nonlinear Powell–Eyring terms model the non-Newtonian nature of the fluid, incorporating the effects of relaxation and retardation parameters.

- **Energy equation**

$$u\frac{\partial T}{\partial x}+v\frac{\partial T}{\partial y}=\mu D_B\frac{\partial \hat{C}}{\partial y}\frac{\partial T}{\partial y}+\mu\frac{D_T}{T_\infty}\left(\frac{\partial T}{\partial y}\right)^2+\alpha\frac{\partial^2 T}{\partial y^2}-\frac{1}{\rho c_p}\frac{\partial q}{\partial y}+\frac{B^2\sigma}{\rho c_p}u^2. \tag{2.3}$$

The first two terms on the left represent thermal convection, while the first term on the right expresses heat conduction within the fluid. The second term represents viscous dissipation, which converts kinetic energy into internal energy due to fluid friction. The third term accounts for Joule heating produced by the magnetic field. Finally, $\partial q/\partial y$ is the divergence of the radiative heat flux, incorporated using the Rosseland approximation.

- **Nanoparticle concentration equation**

$$u\frac{\partial C}{\partial x}+v\frac{\partial C}{\partial y}=D_B\frac{\partial^2 C}{\partial y^2}+\frac{D_T}{T_\infty}\frac{\partial^2 T}{\partial y^2}. \tag{2.4}$$

The convective terms on the left describe the transport of nanoparticles due to bulk motion, while the first term on the right denotes Brownian diffusion (random motion of nanoparticles). The second term represents thermophoretic diffusion, where temperature gradients drive nanoparticle motion.

- **Boundary conditions**

The velocity, temperature, and concentration are specified at the wall and approach free-stream values as $y\to\infty$. Typically,

$$u=U_w(x),\quad v=0,\quad T=T_w,\quad C=C_w\quad \text{at } y=A(x+a)^{\frac{1-n}{2}}, \tag{2.5}$$

$$u\to 0,\quad T\to T_\infty,\quad C\to C_\infty\quad \text{as } y\to\infty. \tag{2.6}$$

These ensure that the surface stretching, thermal, and concentration conditions are correctly imposed.

The boundary conditions employed in this study are physically appropriate because they reflect the geometry and physics of a Powell–Eyring nanofluid flowing over a nonlinearly stretching sheet of variable thickness. At the wall, the conditions

$$u=U_w(x),\qquad v=0,\qquad T=T_w,\qquad C=C_w$$

ensure that the fluid adheres to the stretching surface, satisfies the no-penetration requirement, and is subjected to prescribed temperature and nanoparticle concentration. These conditions are standard in stretching-sheet flow problems and accurately model industrial processes such as extrusion, polymer stretching, and metal forming, where the surface motion and thermal state are controlled. Far from the sheet, the conditions

$$u\to 0,\qquad T\to T_\infty,\qquad C\to C_\infty,\qquad \text{as } y\to\infty,$$

represent a quiescent ambient fluid at free-stream temperature and concentration. These conditions ensure that the effect of the stretching sheet diminishes sufficiently far from the wall and that the flow merges smoothly into the stationary outer fluid, which is essential for a realistic boundary-layer formulation. The chosen boundary conditions capture the essential physics of the stretching sheet problem, enforce proper asymptotic behavior away from the surface, and provide a consistent framework for reducing the governing equations to solvable similarity forms. Here, u and v represent the velocity components in the x and y directions, respectively. The parameters μ, β, and c denote the dynamic viscosity and material constants. We define $\nu=\mu/\rho$ as the kinematic viscosity, σ as the electrical conductivity of the fluid, α as the thermal diffusivity, ρ as the density, and c_P as the specific heat. The parameters D_B and D_T correspond to the Brownian motion and thermophoresis effects, respectively. The temperature and nanoparticle concentration are denoted by T and C, with T_w and T_∞ representing the surface and ambient temperatures, and C_w and C_∞ representing the sheet and ambient nanoparticle concentrations. The radiative heat flux is modeled using the Rosseland approximation as

$$q=-\frac{4\sigma^*}{3k_1}\frac{\partial T^4}{\partial y}, \tag{2.7}$$

where σ^* is the Stefan–Boltzmann constant and k_1 is the mean absorption coefficient. By applying a Taylor series expansion, we approximate

$$T^4\approx 4T_\infty^3 T-3T_\infty^4. \tag{2.8}$$

Substituting Eq. (2.8) into Eq. (2.7) yields

$$q=-\frac{16\sigma^* T_\infty^3}{3k_1}\frac{\partial T}{\partial y}. \tag{2.9}$$

Thus, Eq. (2.3) becomes

$$u\frac{\partial T}{\partial x}+v\frac{\partial T}{\partial y}=\mu D_B\frac{\partial \hat{C}}{\partial y}\frac{\partial T}{\partial y}+\mu\frac{D_T}{T_\infty}\left(\frac{\partial T}{\partial y}\right)^2+\alpha\frac{\partial^2 T}{\partial y^2}+\frac{16\sigma^* T_\infty^3}{3k_1\rho c_p}\frac{\partial T^2}{\partial y^2}+\frac{B^2\sigma}{\rho c_p}u^2, \tag{2.10}$$

The similarity transformations reduce the continuity, momentum, energy, and concentration equations into a dimensionless form that depends on parameters such as the magnetic field strength, wall thickness, and thermophysical properties of the nanofluid. We use the following transformations

$$\vartheta=\sqrt{\left(\frac{n+1}{2\nu}\right)U_0(x+a)^{n-1}}\,y,\quad u=U_0(x+a)^n f'(\vartheta), \tag{2.11}$$

$$\Theta(\vartheta)=\frac{T-T_\infty}{T_w-T_\infty},\quad \Phi(\vartheta)=\frac{C-C_\infty}{C_w-C_\infty}, \tag{2.12}$$

$$v=-\sqrt{\left(\frac{n+1}{2}\right)U_0\nu(x+a)^{n-1}}\left[F(\vartheta)+\frac{n-1}{n+1}\vartheta F'(\vartheta)\right]. \tag{2.13}$$

Using these transformations, the governing equations reduce to

$$F'''=\frac{2nF'^2}{(n+1)(1+M)}+\left(\frac{M(n+1)\lambda}{2(1+M)}\right)F'^2F'''-\frac{FF''}{M+1}+\frac{2H^2F'}{(n+1)(1+M)}, \tag{2.14}$$

$$\left(3+\frac{4R}{3\mathrm{Pr}}\right)\Theta''+\mathrm{Pr}F\Theta'+Nb\Phi'\Theta'+Nt(\Theta')^2+H^2\mathrm{Pr}\,\mathrm{Ec}(F')^2=0, \tag{2.15}$$

$$\Phi''+\mathrm{Pr}\,\mathrm{Le}F\Phi'+\left(\frac{Nt}{Nb}\right)\Theta''=0, \tag{2.16}$$

with boundary conditions

$$F(\alpha)=\frac{1-n}{1+n}\alpha,\qquad F'(\alpha)=1, \tag{2.17}$$

$$\Theta(\alpha)=1,\qquad \Phi(\alpha)=1, \tag{2.18}$$

$$F'(\infty)\to 0,\qquad \Theta(\infty)\to 0,\qquad \Phi(\infty)\to 0. \tag{2.19}$$

To further simplify the governing equations, we introduce the following transformations

$$F(\vartheta)=f(\vartheta-\alpha)=f_1(\zeta),\quad \Theta(\vartheta)=\Theta(\vartheta-\alpha)=f_2(\zeta),\quad \Phi(\vartheta)=\Phi(\vartheta-\alpha)=f_3(\zeta), \tag{2.20}$$

Therefore, the simplified form of the governing equations becomes

$$f_1'''=\frac{2nf_1'^2}{(n+1)(1+M)}+\left(\frac{M(n+1)\lambda}{2(1+M)}\right)f_1'^2f_1'''-\frac{f_1f_1''}{M+1}+\frac{2H^2f_1'}{(n+1)(1+M)}, \tag{2.21}$$

$$\left(3+\frac{4R}{3\mathrm{Pr}}\right)f_2''+\mathrm{Pr}f_1f_2'+Nbf_3'f_2'+Nt(f_2')^2+H^2\mathrm{Pr}\,\mathrm{Ec}(f_1')^2=0, \tag{2.22}$$

$$f_3''+\mathrm{Pr}\,\mathrm{Le}f_1f_3'+\left(\frac{Nt}{Nb}\right)f_2''=0, \tag{2.23}$$

with boundary conditions

$$f_1(0)=\frac{1-n}{1+n}\alpha,\qquad f_1'(0)=1, \tag{2.24}$$

$$f_2(0)=1,\qquad f_3(0)=1, \tag{2.25}$$

$$f_1'(\infty)\to 0,\qquad f_2(\infty)\to 0,\qquad f_3(\infty)\to 0, \tag{2.26}$$

Table 1
Parameters used in the model.

Parameter	Description
u and v	Velocity components in the x and y directions
μ	Dynamic viscosity
β	Material constant
c	Material constant
ν	kinematic viscosity
σ	Electrical conductivity of the fluid
α	Thermal diffusivity
ρ	Density
c_p	Specific heat
D_B	Brownian motion parameter
D_T	Thermophoresis effects parameter
T	Temperature
C	Nanoparticle concentration
T_w	Surface temperatures
T_∞	Ambient temperatures
C_w	Sheet nanoparticle concentrations
C_∞	Ambient nanoparticle concentrations
σ^*	Stefan–Boltzmann constant
k_1	Mean absorption coefficient
H	Magnetic parameter
M	Fluid parameter,
λ	Fluid parameter
R	Radiation parameter
Le	Lewis number
Pr	Prandtl number
Ec	Eckert number
N_t	Thermophoresis parameter
N_b	Brownian motion parameter
U_0	Reference velocity
a	Positive constant
n	Characterizes the degree of nonlinearity
$\delta(x)$	Surface thickness
δ_0	Reference thickness

where $H = \frac{2\sigma B^2}{(n+1)U_0(x+a)^{m-1}\rho}$, $M = \frac{1}{\mu\beta c}$, $\lambda = \frac{a^3 x^2}{2C^2\nu}$, $R = \frac{4\sigma^* T_\infty^3}{k_1 \rho_f c_f \alpha}$, $\mathrm{Le} = \frac{\alpha}{D_B}$, $\mathrm{Pr} = \frac{\nu}{\alpha}$, $\mathrm{Ec} = \frac{\mu D_B C_\infty}{\nu}$, $N_t = \frac{\mu D_T(T_w - T_\infty)}{\nu T_\infty}$, and $N_b = \frac{\mu D_B(C_w - C_\infty)}{\nu}$. The dimensionless forms of the physical quantities, namely the skin friction, Sherwood number, and local Nusselt number, are expressed as follows

$$C_f Re_x^{\frac{1}{2}} = \sqrt{2(n+1)}\left((1+M)f_1''(0) - \frac{(n+1)M\lambda}{6} f_1''^3(0)\right), \tag{2.27}$$

$$Sh_x Re_x^{-\frac{1}{2}} = -\sqrt{\frac{n+1}{2}}\, f_3'(0), \tag{2.28}$$

$$Nu_x Re_x^{-\frac{1}{2}} = -\sqrt{\frac{n+1}{2}}\, f_2'(0), \tag{2.29}$$

where R_e is the local Reynold number. The parameters used in deriving the system of ordinary boundary value problems (2.21)–(2.26) are summarized in Table 1.

The present mathematical model, while effective for capturing the fundamental behavior of magnetohydrodynamic Powell–Eyring nanofluid flow, is subject to several limitations.

1. The analysis is restricted to a two-dimensional, steady, laminar boundary-layer flow over a stretching sheet. Many industrial processes involve three-dimensional effects, turbulence, unsteady motion, and more complex geometries that are not captured by the current formulation.
2. The nanofluid is modeled using standard Brownian motion and thermophoresis effects. Phenomena such as nanoparticle agglomeration, sedimentation, particle–fluid slip, or variations in particle size and shape are neglected, although they may significantly influence real nanofluid transport behavior.
3. Fluid properties such as viscosity, thermal conductivity, and specific heat are assumed constant. In practical applications, these properties often vary with temperature, concentration, or magnetic field strength, which may alter the heat and mass transfer characteristics.
4. The rheological description is restricted to the Powell–Eyring constitutive equation, which accounts for shear-thinning behavior but does not represent viscoplastic, shear-thickening, or yield-stress fluids that frequently occur in industrial operations.
5. The analysis assumes prescribed wall temperature and nanoparticle concentration. More realistic conditions – such as convective heating, radiative flux boundaries, slip velocity, or surface roughness – are not included.

These limitations highlight opportunities for future work, including the incorporation of variable properties, three-dimensional effects, more complex rheological models, and experimental validation to enhance the applicability of the present framework.

One significant industrial application of Powell–Eyring fluids arises in the processing of polymer melts. Many molten polymers exhibit pronounced shear-thinning behavior, for which classical Newtonian or simple power-law models fail to provide accurate rheological predictions. During operations such as film blowing, fiber spinning, injection molding, and sheet extrusion, the material experiences high shear rates that lead to substantial reductions in viscosity. The Powell–Eyring model is particularly suitable for these processes because it captures nonlinear, rate-dependent viscosity while avoiding the mathematical singularities that occur in other non-Newtonian models at low shear rates. This provides a more realistic description of polymer melt behavior during stretching, coating, and shaping operations. Accurate modeling of such rheology is essential for controlling product thickness, enhancing mechanical performance, optimizing energy usage, and preventing defects such as melt fracture or surface irregularities in industrial polymer manufacturing.

3. Description of the numerical approach

Because the system defined in Eqs. (2.21)–(2.26) is nonlinear, obtaining an exact analytical solution is challenging. Therefore, we employ the modified operational matrix method proposed by Syam et al. [30,31] as a numerical technique. To initiate the procedure, the following variable transformations are introduced.

$$\kappa_1 = f_1, \quad \kappa_2 = \kappa_1', \quad \kappa_3 = \kappa_2', \quad \kappa_4 = f_2, \quad \kappa_5 = \kappa_4', \quad \kappa_6 = f_3, \quad \kappa_7 = \kappa_6'. \tag{3.1}$$

Substituting these transformations into the system of Eqs. (2.21)–(2.26), the governing equations can be reformulated as follows.

$$\kappa_1' = \kappa_2, \quad \kappa_2' = \kappa_3, \quad \kappa_3' = \frac{\frac{2n\kappa_2^2}{(n+1)(1+M)} - \frac{\kappa_1\kappa_3}{M+1} + \frac{2H^2\kappa_2}{(n+1)(1+M)}}{\left(1 - \left(\frac{M(n+1)\lambda}{2(1+M)}\right)\kappa_2^2\right)}, \tag{3.2}$$

$$\kappa_1(0) = \frac{1-n}{1+n}\alpha, \kappa_2(0) = 1, \kappa_3(0) = \omega_1, \tag{3.3}$$

$$\kappa_4' = \kappa_5, \quad \kappa_5' = -\frac{\mathrm{Pr}\kappa_1\kappa_5 + Nb\kappa_7\kappa_5 + Nt(\kappa_5)^2 + H^2\mathrm{Pr}\,\mathrm{Ec}(\kappa_2)^2}{3 + \frac{4R}{3\mathrm{Pr}}}, \tag{3.4}$$

$$\kappa_4(0) = 1, \kappa_5(0) = \omega_2, \tag{3.5}$$

$$\kappa_6' = \kappa_7, \quad \kappa_7' = -\mathrm{PrLe}\kappa_1\kappa_7 + \left(\frac{Nt}{Nb}\right)\frac{\mathrm{Pr}\kappa_1\kappa_5 + Nb\kappa_7\kappa_5 + Nt(\kappa_5)^2 + H^2\mathrm{Pr}\,\mathrm{Ec}(\kappa_2)^2}{3 + \frac{4R}{3\mathrm{Pr}}}, \tag{3.6}$$

$$\kappa_6(0) = 1, \kappa_7(0) = \omega_3. \tag{3.7}$$

The parameters ω_1, ω_2, and ω_3 are determined by solving the system of Eqs. (3.2)–(3.7) under the boundary conditions $\kappa_2(\infty) = 0$, $\kappa_4(\infty) = 0$, and $\kappa_6(\infty) = 0$. The system can be reformulated in matrix form as follows:

$$K' = \Pi(K), \quad K(0) = K_0, \tag{3.8}$$

where

$$K=\begin{bmatrix}\kappa_1\\ \kappa_2\\ \kappa_3\\ \kappa_4\\ \kappa_5\\ \kappa_6\\ \kappa_7\end{bmatrix},\quad K_0=\begin{bmatrix}\frac{1-n}{1+n}\alpha\\ 1\\ \omega_1\\ 1\\ \omega_2\\ 1\\ \omega_3\end{bmatrix},$$

$$\Pi(K)=\begin{bmatrix}\kappa_2\\ \kappa_3\\ \dfrac{\frac{2n\kappa_2^2}{(n+1)(1+M)}-\frac{\kappa_1\kappa_3}{1+M}+\frac{2H^2\kappa_2}{(n+1)(1+M)}}{\left(1-\left(\frac{M(n+1)\lambda}{2(1+M)}\right)\kappa_2^2\right)}\\ \kappa_5\\ -\dfrac{\Pr\kappa_1\kappa_5+Nb\,\kappa_7\kappa_5+Nt\,\kappa_5^2+H^2\Pr\mathrm{Ec}\,\kappa_2^2}{3+\frac{4R}{3\Pr}}\\ \kappa_7\\ -\Pr\mathrm{Le}\,\kappa_1\kappa_7+\left(\frac{Nt}{Nb}\right)\dfrac{\Pr\kappa_1\kappa_5+Nb\,\kappa_7\kappa_5+Nt\,\kappa_5^2+H^2\Pr\mathrm{Ec}\,\kappa_2^2}{3+\frac{4R}{3\Pr}}\end{bmatrix}. \tag{3.9}$$

Following the numerical approach outlined in [30–32], the solution vector is expanded as a finite series:

$$K(\zeta)=\sum_{i=0}^{L}K_i\psi_i(\zeta), \tag{3.10}$$

where the set of functions $\{\psi_0(\zeta),\psi_1(\zeta),\dots,\psi_L(\zeta)\}$ denotes the block pulse functions defined by

$$\psi_i(\zeta)=\begin{cases}1, & \zeta_i\le\zeta<\zeta_{i+1},\\ 0, & \text{otherwise.}\end{cases} \tag{3.11}$$

Here, $\{\zeta_0,\zeta_1,\dots,\zeta_L\}$ represents a uniform partition of the interval $[0,\zeta_{\max}]\approx[0,\infty)$ with a constant step size Δ. Substituting this representation into Eq. (3.8) yields the following integral form:

$$K(\zeta)=K_0+\int_0^{\zeta}\Pi(K(\epsilon))\,d\epsilon. \tag{3.12}$$

At the discrete collocation points ζ_j, where $j=1,2,\dots,L$, the block pulse functions satisfy

$$\psi_i(\zeta_j)=\begin{cases}1, & j=i,\\ 0, & \text{otherwise,}\end{cases} \tag{3.13}$$

which implies

$$K(\zeta_j)=\sum_{i=0}^{L}K_i\psi_i(\zeta_j)=K_j. \tag{3.14}$$

Thus, the recursive form of the solution can be expressed as

$$\begin{aligned}K_j &= K_0+\sum_{i=0}^{j-1}\int_{\eta_i}^{\eta_{i+1}}\Pi(K(\epsilon))\,d\epsilon\\ &= K_0+\Delta\sum_{i=0}^{j-1}\Pi(K_i).\end{aligned} \tag{3.15}$$

Remark 3.1. The following key points are worth noting:

1. Computing the coefficients of the approximation in (3.10) using the conventional OMM involves constructing operational matrices to formulate a nonlinear algebraic system. Such a system may comprise more than one hundred equations, resulting in high computational cost and considerable processing time. Moreover, obtaining an analytical solution is typically impractical, and numerical techniques must be employed to approximate the results. This dependence on numerical computation can lead to significant errors, with the standard OMM often producing inaccuracies exceeding 10^{-5} when applied to nonlinear problems in physical and engineering applications.
2. Conversely, the proposed modified approach for determining the coefficients in (3.10), as expressed in Eq. (3.15), adopts a forward iterative strategy that removes the need to solve large systems of equations. In this scheme, each K_i is explicitly defined in terms of $K_0,K_1,\dots,K_{i-1}$. As a result, the modified OMM is easier to implement, more computationally efficient, and achieves higher accuracy by avoiding the direct solution of nonlinear systems.
3. When compared with other numerical techniques, such as BVP4C, RKF45, the Variational Iteration Method (VIM), and the Adomian Decomposition Method (ADM), the proposed approach demonstrates greater simplicity, lower computational cost, and improved accuracy. A comprehensive evaluation of the method's performance in terms of speed, cost, and precision is provided in [30,31].

Further details regarding error estimation and convergence behavior can be found in [30]. As evident from Eq. (3.15), the proposed method is direct, iterative, and computationally efficient for solving nonlinear systems, providing higher accuracy and shorter execution time than conventional numerical schemes.

4. Error analysis

Consider a function $K\in L^2([0,\zeta_{\max}))$ with the norm defined as

$$\|K\|=\sqrt{\int_0^{\zeta_{\max}}|K(\eta)|^2\,d\eta}. \tag{4.1}$$

According to Eq. (3.10), the function $K(\zeta)$ can be approximated by the truncated expansion

$$K(\zeta)=\sum_{i=0}^{L}K_i\psi_i(\zeta), \tag{4.2}$$

where L denotes the truncation order. The coefficients K_i are determined from

$$K_i=\frac{1}{\Delta}\int_0^{\zeta_{\max}}K(\eta)\psi_i(\eta)\,d\eta. \tag{4.3}$$

The following theorem demonstrates that the coefficients K_i obtained from Eq. (4.3) minimize the mean-square error of the approximation.

Theorem 4.1. *Let $K\in L^2([0,\zeta_{max}))$ and let $K_L(\zeta)$ be its truncated approximation given by Eq. (4.2). The mean-square error is defined as*

$$\mathcal{F}(K_0,K_1,\dots,K_L)=\int_0^{\zeta_{max}}\left\|K(\eta)-K_L(\eta)\right\|^2\,d\eta,$$

and it attains its minimum when Λ_i satisfies Eq. (4.3) for all $i=0,1,\dots,L$.

Proof. For $i=0,1,\dots,L$, the first derivative of $\mathcal{F}$ with respect to K_i is

$$\frac{\partial\mathcal{F}}{\partial K_i}=2\int_0^{\zeta_{\max}}\left(K(\eta)-K_L(\eta)\right)\psi_i(\eta)\,d\eta=2\left(\int_0^{\zeta_{\max}}K(\eta)\psi_i(\eta)\,d\eta-\Delta K_i\right)=0.$$

Hence,

$$K_i=\frac{1}{\Delta}\int_0^{\zeta_{\max}}K(\eta)\psi_i(\eta)\,d\eta.$$

The second derivative of $\mathcal{F}\mathcal{G}$ is

$$\frac{\partial^2\mathcal{F}}{\partial K_i\partial K_j}=\begin{cases}2\Delta, & \text{if } i=j,\\ 0, & \text{otherwise,}\end{cases}\qquad 0\le i,j\le L.$$

The determinant of the corresponding Hessian matrix is

$$\begin{vmatrix}2\Delta & 0 & \dots & 0\\ 0 & 2\Delta & \dots & 0\\ \vdots & \vdots & \ddots & \vdots\\ 0 & 0 & \dots & 2\Delta\end{vmatrix}=(2\Delta)^{i+1}>0,$$

Table 2
The L_2-truncation error for different values of M, n, λ, H, R, Pr, Nt, Nb, Ec, Le, and α.

Pr	n	Nb	Nt	Le	α	λ	M	H	R	Ec	G_e	SPU time (s)
1.2	0.1	0.5	0.5	0.3	0.2	0.2	0.1	0.1	0.1	0.1	2.35×10^{-13}	7.10
1.4	0.2	0.4	0.3	0.33	0.3	0.3	0.1	0.2	0.2	0.1	2.89×10^{-13}	7.20
1.6	0.3	0.7	0.1	0.35	0.4	0.4	0.2	0.3	0.2	0.4	3.11×10^{-13}	7.2
1.8	0.4	0.8	0.3	0.4	0.3	0.35	0.5	0.3	0.2	0.1	3.12×10^{-13}	6.9
2	0.4	0.3	0.4	0.35	0.4	0.5	0.3	0.2	0.3	0.4	2.99×10^{-13}	6.8
2.1	0.2	0.5	0.5	0.3	0.5	0.4	0.3	0.3	0.4	0.2	2.88×10^{-13}	7.0

confirming that the Hessian is positive definite. Therefore, $\mathcal{F}$ is minimized when each K_i satisfies Eq. (4.3).

Next, we examine the mean-square error associated with approximating $K(\zeta)$ over $[0,\zeta_{\max})$.

Theorem 4.2. *Assume that $K(\zeta)$ is differentiable on $[0,\zeta_{max})$ and satisfies*

$$|K'(\zeta)| \le \mathcal{A}, \tag{4.4}$$

for some positive constant $\mathcal{A}$. Then, the mean-square error satisfies the bound

$$\|\mathcal{F}\|^2 \le C\Delta^2, \tag{4.5}$$

where $\mathcal{F}(K) = K(\zeta) - K_L(\zeta)$ for $\zeta \in [0,\zeta_{max})$, $\Delta = \frac{\zeta_{max}}{L}$, and C is a positive constant.

Proof. Let $\zeta_i = i\Delta$ and $\mathcal{F}_i = [\zeta_i,\zeta_{i+1})$, where $\Delta = \frac{\zeta_{\max}}{L}$. Using the mean value theorem and Eq. (4.3), we obtain:

$$\begin{aligned} K_L(\zeta) &= K_i, \quad \zeta \in [\zeta_i,\zeta_{i+1}),\\ &= \frac{1}{\Delta}\int_{\zeta_i}^{\zeta_{i+1}} K(t)\,dt,\\ &= K(\varrho_i), \quad \varrho_i \in [\zeta_i,\zeta_{i+1}), \quad i = 0,1,\dots,L. \end{aligned}$$

Applying the mean value theorem to the error term yields:

$$\begin{aligned} \|\mathcal{F}\|^2 &= \int_0^{\zeta_{\max}} \|K(\zeta) - K_L(\zeta)\|^2\,d\zeta\\ &= \sum_{i=0}^{L}\int_{\zeta_i}^{\zeta_{i+1}} \|K(\zeta) - K_L(\zeta)\|^2\,d\zeta\\ &= \Delta\sum_{i=0}^{L}\|K(\omega_i) - K(\varrho_i)\|^2, \end{aligned}$$

where $\omega_i, \varrho_i \in [\zeta_i,\zeta_{i+1})$. Using Eq. (4.4) and the Lipschitz continuity of $K'(\zeta)$, we obtain

$$\begin{aligned} \|\mathcal{F}\|^2 &\le \Delta\mathcal{A}^2\sum_{i=0}^{L}(\omega_i - \varrho_i)^2\\ &\le \Delta\mathcal{A}^2\sum_{i=0}^{L}\Delta^2\\ &= L\mathcal{A}^2\Delta^3 = (\zeta_{\max}\mathcal{A}^2)\Delta^2 = C\Delta^2, \end{aligned}$$

where $C = \mathcal{A}^2\zeta_{\max}$. □

This theorem shows that the mean-square error of the approximation is of order $\mathcal{O}(\Delta^2)$.

In the following theorem, we establish the existence and uniqueness of the solution.

Theorem 4.3. *Let $\Pi \in H = C((0,\zeta_{max}),\mathbb{R}^3)$ be a matrix function bounded by a positive constant Λ. Then, Problem (3.8) admits a unique solution if*

$$\Lambda\,\zeta_{max} < 1. \tag{4.6}$$

Proof. We rewrite Eq. (3.8) in its equivalent integral form:

$$\begin{aligned} K(\zeta) &= K(0) + \int_0^{\zeta}\Pi(K(r))\,dr\\ &= K_0 + \int_0^{\zeta}\Pi(K(r))\,dr. \end{aligned} \tag{4.7}$$

Define the operator Σ by

$$\Sigma(K) = K_0 + \int_0^{\zeta}\Pi(K(r))\,dr.$$

Then, for any $K_1, K_2 \in H$, we have

$$\begin{aligned} \|\Sigma(K_1) - \Sigma(K_2)\| &= \left\|\int_0^{\zeta}\big(\Pi(K_1(r)) - \Pi(K_2(r))\big)\,dr\right\|\\ &\le \int_0^{\zeta}\|\Pi(K_1(r)) - \Pi(K_2(r))\|\,dr\\ &\le \zeta\,\|\Pi\|\,\|K_1 - K_2\|\\ &\le \Lambda\,\zeta_{\max}\,\|K_1 - K_2\|. \end{aligned}$$

Since $\Lambda\,\zeta_{\max} < 1$, the operator Σ is a contraction on H. Therefore, by the Banach fixed-point theorem, Problem (3.8) admits a unique solution. □

5. Validation of the method

Due to the nonlinear nature of the boundary value problem (2.21)–(2.26), an exact solution cannot be obtained. Instead, we apply the modified OMM to derive an approximate analytical solution, as expressed in Eq. (3.8). To do that, we define the L_2-truncation error, which will serve as the error tolerance and is given in Eq. (5.1). In addition, we fix the value of the step size. From now on, the step size is $\Delta = 10^{-3}$. To assess how well the approximate solution aligns with the exact one, we calculate the absolute error function

$$\|\, K' - \Pi(K)\,\|_E^2\ .$$

This error, however, provides only a local measure, as it applies to each specific ζ within the domain. To avoid this, we compute the global error as shown in Eq. (5.1), referred to as the L_2-truncation error. This global error measure offers a more reliable assessment compared to the absolute error. For the purposes of validation, the L_2-truncation error is defined as follows:

$$G_e = \sqrt{\int_0^{\zeta_{max}} \|K'(\eta) - \Pi(K(\eta))\|^2\,d\eta}. \tag{5.1}$$

Here, $\|.\|_E$ represents the Euclidean norm. Table 2 presents the computed truncation errors for various parameter choices, including M, n, λ, H, R, Pr, Nt, Nb, Ec, Le, and α.

Table 3 compares the boundary conditions for $M = 0.2$, $n = 0.5$, $\lambda = 0.2$, $H = 0.2$, $R = 0.2$, Pr $= 2$, Nt $= 0.5$, Nb $= 0.5$, Ec $= 0.1$, Le $= 3$, and $\alpha = 0.5$. with their exact values, given in Eqs. (2.21)–(2.26). These comparisons demonstrate that the shooting method used is functioning correctly, as the approximate values closely match the exact boundary conditions. The results are shown in Table 3.

Tables 4–6 present the effects of varying flow parameters on the skin friction coefficient, the Nusselt number, and the Sherwood number, respectively.

Table 3
Boundary conditions for $M = 0.2$, $n = 0.5$, $\lambda = 0.2$, $H = 0.2$, $R = 0.2$, $\Pr = 2$, $\mathrm{Nt} = 0.5$, $\mathrm{Nb} = 0.5$, $\mathrm{Ec} = 0.1$, $\mathrm{Le} = 3$, and $\alpha = 0.5$.

Condition	Numerical value	Exact value
$\left\lvert f_1(0) - \frac{1-n}{1+n}\alpha \right\rvert$	0	0
$\lvert f_1'(0) - 1\rvert$	5.27×10^{-15}	0
$\lvert f_2(0) - 1\rvert$	1.84×10^{-15}	0
$\lvert f_3(0) - 1\rvert$	1.19×10^{-15}	0
$\lvert f_1'(\infty)\rvert$	0	0
$\lvert f_2(\infty)\rvert$	0	0
$\lvert f_3(\infty)\rvert$	0	0

Table 4
Effect of varying flow parameters on the skin friction coefficient.

N	M	λ	H	α	$\frac{1}{2}C_f Re_x^{1/2}$ [35]	$\frac{1}{2}C_f Re_x^{1/2}$ (OMM)
0.1	1.2	0.1	0.1	0.9	3.2250	3.22500
				1.0	3.0619	3.06200
				1.1	2.9580	2.95810
0.1	1.2	0.1	0.1	0.9	3.2225	3.22250
	1.5				3.5080	3.50801
	1.8				3.7924	3.79239
1.2	0.1				3.2250	3.22501
	0.2				3.1348	3.13480
	0.5				2.4692	2.46920
0.1	0.3				2.6685	2.66850
	0.4				3.7797	3.77971
	0.5				5.9973	5.99730
0.1	0.7				0.0093	0.00929
	0.9				3.2225	3.22250
	1.2				3.4461	3.44609

6. Analysis of results and discussion of results

This section is organized into two parts. The first part presents an analysis of the obtained results, while the second subsection provides a discussion of the main findings.

6.1. Analysis of results

The physical model involves several key dimensionless parameters that govern the transport behavior of the Powell–Eyring nanofluid. These include the thermal diffusivity parameter α, magnetic parameter H, fluid parameters M and λ, nonlinearity index n, radiation parameter R, Prandtl number Pr, Brownian motion parameter N_b, thermophoresis parameter N_t, Eckert number Ec, and Lewis number Le. Each parameter represents a distinct physical mechanism: M, λ, and n characterize the nonlinear stretching and rheology of the Powell–Eyring model; H, Ec, and R account for magnetic effects, viscous dissipation, and radiative heat transfer; while Pr, N_b, N_t, and Le regulate thermal and solutal transport through thermal diffusion, Brownian motion, thermophoresis, and species diffusivity, respectively. The parameter values used in the simulations were selected based on ranges commonly reported in the literature on nanofluid flow, MHD transport, and Powell–Eyring fluid models. For the velocity-related parameters, we considered the ranges

$$0.1 \le M \le 1.7, \qquad 0.1 \le \lambda \le 0.5, \qquad 0.1 \le n \le 0.5,$$

which correspond to moderate non-Newtonian characteristics typically used in earlier numerical studies. Thermal and concentration transport parameters were chosen within the realistic ranges

$$1.1 \le \Pr \le 1.8, \qquad 0.1 \le N_b \le 0.7, \qquad 0.1 \le N_t \le 0.7, \qquad 1.8 \le Le \le 3.0,$$

reflecting the thermophysical properties of water-based nanofluids. The Eckert and radiation parameters were taken as

$$0.1 \le Ec \le 0.4, \qquad 0.1 \le R \le 0.4,$$

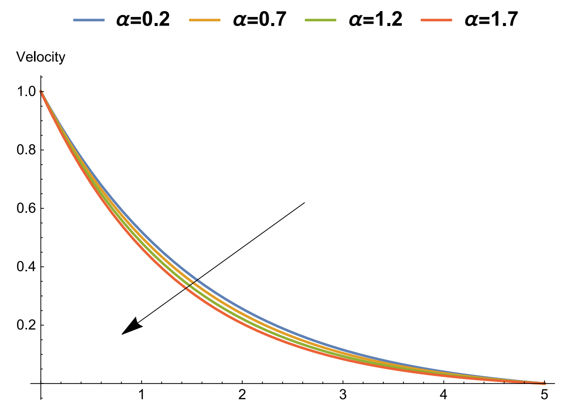

Fig. 2. Influence of the thermal diffusivity α on the velocity.

capturing realistic levels of viscous heating and radiative effects. The magnetic parameter H was varied within

$$0.2 \le H \le 1.7,$$

representing moderate Hartmann numbers applicable to electrically conducting nanofluids. These parameter ranges were selected to ensure physically meaningful simulations and to permit a systematic exploration of the dominant transport mechanisms. By varying each parameter within its realistic operational window, we were able to analyze its influence on the velocity, temperature, and concentration fields, as illustrated in Figs. 2–20. This approach provides a comprehensive understanding of how magnetic forces, radiation, viscous dissipation, Brownian diffusion, and thermophoresis collectively shape the transport behavior of the nanofluid. To gain a deeper understanding of the flow behavior and the corresponding numerical results, a graphical analysis is conducted to illustrate the influence of the key parameters in System (2.21)–(2.26) on the solution, as presented in Figs. 2–20.

Figs. 2–6 show the effects of thermal diffusivity α, fluid parameters λ and M, magnetic parameter H, and the nonlinearity index n on the velocity profile. In these figures, the following parameter values are used: $M = 1.5$, $n = 0.5$, $\lambda = 0.1$, $H = 0.5$, $R = 0.5$, $\Pr = 1$, $\mathrm{Nt} = 0.3$, $\mathrm{Nb} = 0.3$, $\mathrm{Ec} = 0.5$, $\mathrm{Le} = 1$, and $\alpha = 0.5$. In each figure, one parameter is varied while the others are kept constant to illustrate its specific effect on the velocity distribution.

The effects of the radiation parameter R, the Prandtl number Pr, the Brownian motion parameter Nb, the thermophoresis parameter Nt, the magnetic parameter H, and the Eckert number Ec on the temperature distribution are illustrated in Figs. 7–12. Unless otherwise specified in the figure captions, the parameters used in these figures are set as follows: $M = 0.1$, $n = 0.1$, $\lambda = 0.1$, $H = 0.1$, $R = 0.1$, $\Pr = 1.2$, $\mathrm{Nt} = 0.2$, $\mathrm{Nb} = 0.2$, $\mathrm{Ec} = 0.2$, $\mathrm{Le} = 0.2$, and $\alpha = 0.2$.

The effects of the Lewis number Le, the Brownian motion parameter Nb, the thermophoresis parameter Nt, and the Prandtl number Pr on the concentration are illustrated in Figs. 13–16. Unless otherwise specified in the figure captions, the parameters are set as follows: $M = 0.2$, $n = 0.5$, $\lambda = 0.2$, $H = 0.2$, $R = 0.2$, $\Pr = 2$, $\mathrm{Nt} = 0.5$, $\mathrm{Nb} = 0.5$, $\mathrm{Ec} = 0.1$, $\mathrm{Le} = 3$, and $\alpha = 0.5$.

Figs. 17–20 illustrate the effects of the thermophoresis parameter Nt and the Prandtl number Pr on the Nusselt number, the thermal diffusivity parameter α on the skin friction coefficient, and the Lewis number Le on the Sherwood number, respectively.

6.2. Discussion of results

This subsection provides a discussion of the results presented in the previous section. From the obtained figures, the following observations are made:

Table 5
Effect of varying flow parameters on the Magnitude of Nusselt number.

Nt	Nb	Ec	M	R	Pr	$Nu_x Re_x^{-1/2}$ [35]	$Nu_x Re_x^{-1/2}$ (OMM)
0.1	0.2	0.01	1.2	0.1	2.0	1.5149	1.51489
0.2						1.4805	1.48050
0.3						1.4458	1.44580
0.1	0.1					1.5739	1.57390
0.2						1.5149	1.514901
0.3						1.4565	1.45650
0.1		0.01				1.5739	1.573899
		0.03				1.4403	1.44029
		0.05				1.3068	1.30680
0.01			1.2			1.5739	1.57390
			1.5			1.5204	1.52040
			1.8			1.4177	1.41770
1.2			0.1	0.1		1.5739	1.573899
				0.2		1.4133	1.413299
				0.3		1.2799	1.279901
0.1					1.5	1.1897	1.18970
					1.8	1.4239	1.42390
					2.0	1.5739	1.57390

Table 6
Effect of varying flow parameters on the Sherwood number.

Le	Pr	Nt	Nb	$Sh_x Re_x^{-1/2}$ [35]	$Sh_x Re_x^{-1/2}$ (OMM)
0.2	1.8	0.1	0.1	0.9466	0.946601
0.3				0.8409	0.840900
0.4				0.6983	0.698299
0.2	1.5			0.7303	0.730300
1.8				0.9466	0.946600
2.0				1.0800	1.08000‘
1.8	0.1			0.9466	0.946600
	0.2			2.2325	2.232500
	0.3			3.4514	3.451400
0.1	0.1			0.9466	0.946599
	0.2			0.2453	0.245301
	0.3			0.0116	0.011599

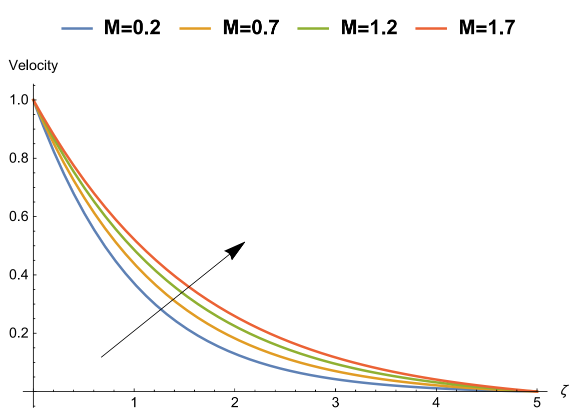

Fig. 3. Influence of the fluid parameter M on the velocity.

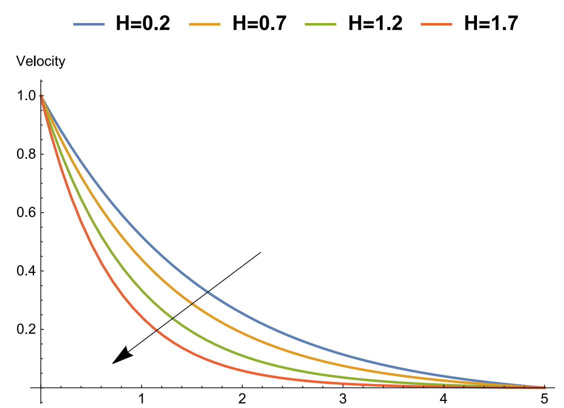

Fig. 4. Influence of the magnetic parameter H on the velocity.

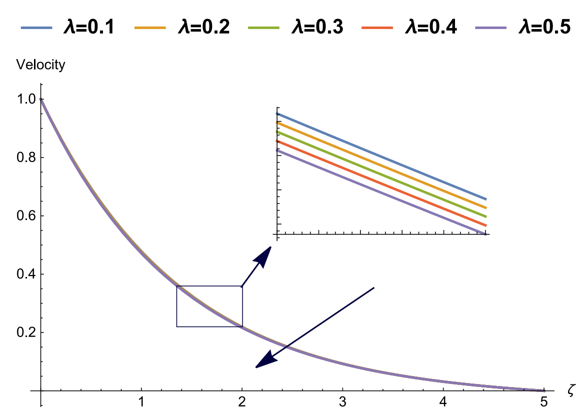

Fig. 5. Influence of the fluid parameter λ on the velocity.

- Figs. 2–6 show the effects of thermal diffusivity α, fluid parameters λ and M, magnetic parameter H, and the nonlinearity index n on the velocity profile. In these figures, the following parameter values are used: $M = 1.5$, $n = 0.5$, $\lambda = 0.1$, $H = 0.5$, $R = 0.5$, $\mathrm{Pr} = 1$, $\mathrm{Nt} = 0.3$, $\mathrm{Nb} = 0.3$, $\mathrm{Ec} = 0.5$, $\mathrm{Le} = 1$, and $\alpha = 0.5$. In each figure, one parameter is varied while the others are kept constant to illustrate its specific effect on the velocity distribution.
- Fig. 2 demonstrates that, as thermal diffusivity α increases, the velocity profile decreases until $\tau = 5$ for values of thermal diffusivity $\alpha = 0.2, 0.7, 1.2$ and 1.7. Increasing the thermal diffusivity α in the present model significantly reduces the velocity profile across the boundary layer up to the similarity coordinate $\tau = 5$. This reduction is a direct result of the thermal–momentum coupling in the governing equations. A larger α accelerates heat conduction away from the wall, thereby reducing local temperature gradients in the thermal boundary layer. As temperature affects the momentum balance in our formulation, the attenuation of temperature gradients weakens the thermally induced momentum source. This leads to a thinner region of thermally-driven acceleration and a lower velocity profile for the tested values $\alpha = 0.2, 0.7, 1.2$, and 1.7 (as

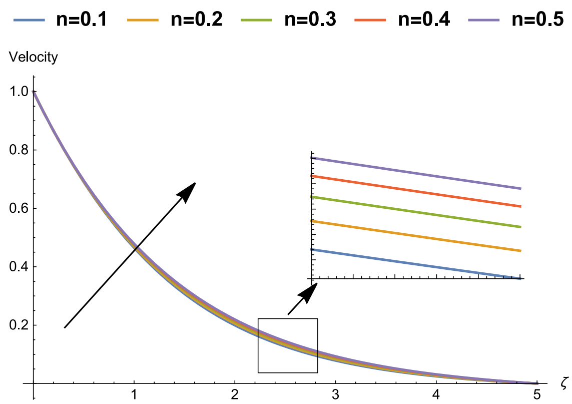

Fig. 6. Influence of the nonlinearity index n on the velocity.

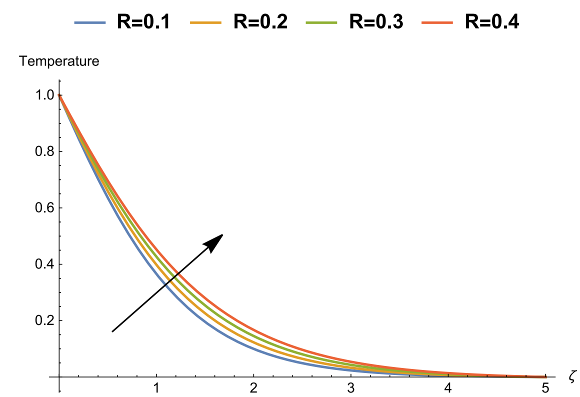

Fig. 7. Influence of the radiation parameter R on the temperature.

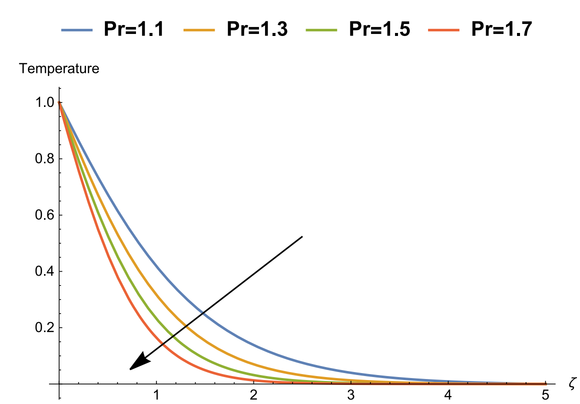

Fig. 8. Influence of the Prandtl parameter Pr on the temperature.

shown for $\tau < 5$). In essence, larger thermal diffusivity smooths temperature differences and diminishes the thermal forcing that would otherwise enhance the flow.

- Fig. 3 demonstrate the effect of the fluid parameter M on the velocity profile. Fig. 3 shows that the velocity profile increases as the fluid parameter M increases until $\tau = 5$ for values of the fluid parameter $M = 0.2, 0.7, 1.2$, and 1.7. The computed results demonstrate that the velocity profile increases with the fluid parameter M (examined for $M = 0.2, 0.7, 1.2$, and 1.7) up to $\tau = 5$. Interpreting M as a parameter that effectively strengthens the fluid's capability to convect momentum, an increase in M augments the convective transport relative to diffusive losses. This is mathematically represented as an increased contribution of terms that drive the axial velocity or as a reduction in the relative magnitude of damping terms. Physically, it means the fluid responds more readily to the surface stretching and body forces in the model. Consequently, higher M values produce larger velocity magnitudes throughout the boundary layer in the region considered.
- Fig. 4 shows the effect of the magnetic parameter H on the velocity profile. Fig. 4 demonstrates that the velocity profile decreases as the magnetic parameter H increases until $\tau = 5$ for values of magnetic parameter $H = 0.2, 0.7, 1.2$, and 1.7. The magnetic parameter H induces a clear retardation of the flow: as H increases (values $H = 0.2, 0.7, 1.2$, and 1.7), the velocity profile decreases up to $\tau = 5$. This behavior is consistent with the classical magnetohydrodynamic (MHD) effect, where an applied magnetic field generates a Lorentz force that opposes the motion of an electrically conducting fluid. In the momentum equation, this appears as an additional damping term proportional to the magnetic strength. Physically, the induced electromagnetic forces act as an extra resistive mechanism, extracting kinetic energy from the flow and therefore reducing velocities throughout the boundary layer. Hence, stronger magnetic fields produce stronger magnetic braking and lower velocity magnitudes in the computed range.
- Fig. 5 shows the effect of the fluid parameter λ on the velocity profile. Fig. 5 demonstrates that the velocity profile decreases as the fluid parameter λ increases until $\tau = 5$ for values of fluid parameter $\lambda = 0.1, 0.2, 0.3$, and 0.5. Raising the fluid parameter λ leads to a decrease in the velocity profile for the tested values $\lambda = 0.1, 0.2, 0.3$, and 0.5 up to $\tau = 5$. In the governing framework used here, λ represents a measure of the fluid's internal resistance or an elasticity/relaxation-related characteristic that increases the effectual hindrance to motion when it grows. An increased λ therefore strengthens the stress (or resistance) terms relative to the driving terms produced by the stretching surface and convective transport. The practical effect is to slow the fluid response, producing reduced velocities across the boundary layer. Thus, larger λ values correspond to stronger resistance and correspondingly lower velocity profiles in the region examined.
- Fig. 6 shows the effect of the nonlinearity index n on the velocity profile. Fig. 6 demonstrates that the velocity profile increases as the nonlinearity index n increases until $\tau = 5$ for values of nonlinearity index $n = 0.1, 0.2, 0.3$, and 0.5. The numerical results indicate that the velocity profile increases with the nonlinearity index n for the chosen set $n = 0.1, 0.2, 0.3$, and 0.5 up to $\tau = 5$. The nonlinearity index modifies how the stretching of the surface translates into momentum input into the fluid: larger n amplifies the effective surface forcing (or redistributes the imposed stretching more strongly into the flow) so that the convective acceleration near the wall is enhanced. From the point of view of the similarity-reduced equations, an increased n strengthens the source-like terms related to surface deformation, yielding a greater momentum transfer into the boundary layer. Therefore, higher values of n produce larger velocities within the region considered.

The effects of the radiation parameter R, the Prandtl number Pr, the Brownian motion parameter Nb, the thermophoresis parameter Nt, the magnetic parameter H, and the Eckert number Ec on the temperature distribution are illustrated in Figs. 7–12. Unless otherwise specified in the figure captions, the parameters used in these figures are set as follows: $M = 0.1$, $n = 0.1$, $\lambda = 0.1$, $H = 0.1$, $R = 0.1$, $\mathrm{Pr} = 1.2$, $\mathrm{Nt} = 0.2$, $\mathrm{Nb} = 0.2$, $\mathrm{Ec} = 0.2$, $\mathrm{Le} = 0.2$, and $\alpha = 0.2$.

- Fig. 7 represents the effect of the radiation parameter R on the temperature distribution. Fig. 7 demonstrates that the temperature distribution increases as the radiation parameter R increases until $\tau = 5$ for values of radiation parameter $R = 0.1, 0.2, 0.3$, and 0.4. The computed profiles show an apparent rise in temperature throughout the thermal boundary layer when the radiation parameter R is increased (examined at $R = 0.1, 0.2, 0.3$, and 0.4) up to $\tau = 5$. Physically, a higher R represents stronger radiative heat transfer into the fluid; this augments the net energy supplied to the boundary layer, elevating local temperatures and widening the thermal layer. In other words, radiation adds an extra mode of energy input that increases the fluid enthalpy and thus raises the temperature distribution for the tested R values.

- Fig. 8 shows the effect of the Prandtl number Pr on the temperature distribution. Fig. 8 demonstrates that the temperature distribution decreases as the Prandtl number Pr increases until $\tau = 5$ for values of Prandtl number $Pr = 1.1, 1.3, 1.5$, and 1.7. The numerical results indicate that the temperature profile decreases as the Prandtl number Pr increases (shown for $Pr = 1.1, 1.3, 1.5$, and 1.7) within $\tau \leq 5$. This behavior follows from the definition of Pr as the ratio of momentum diffusivity to thermal diffusivity: a larger Pr means smaller thermal diffusivity relative to momentum transport, which produces a thinner thermal boundary layer and steeper thermal gradients near the wall but lower temperatures away from the wall. Thus, increasing Pr confines heat closer to the surface and reduces the temperature values in the region plotted, explaining the observed decrease.
- Fig. 9 represents the effect of the Brownian motion parameter Nb on the temperature distribution. Fig. 9 demonstrates that the temperature distribution increases as the Brownian motion parameter Nb increases until $\tau = 5$ for values of Brownian motion parameter $Nb = 0.1, 0.3, 0.5$, and 0.7. Temperature profiles rise when the Brownian motion parameter Nb is increased (examined at $Nb = 0.1, 0.3, 0.5$, and 0.7) up to $\tau = 5$. In the nanofluid model used, Brownian motion quantifies the random motion of nanoparticles, which contributes to enhanced micro-scale energy exchange between particles and base fluid; this augments effective thermal transport and can act as an additional source of thermal energy within the boundary layer. Consequently, larger Nb increases the thermal energy content of the fluid and yields higher temperature distributions for the considered parameter values.
- Fig. 10 shows the effect of the thermophoresis parameter Nt on the temperature distribution. Fig. 10 demonstrates that the temperature distribution increases as the thermophoresis parameter Nt increases until $\tau = 5$ for values of thermophoresis parameter $Nt = 0.1, 0.3, 0.5$, and 1.7. The temperature increases as the thermophoresis parameter Nt is raised (results shown for $Nt = 0.1, 0.3, 0.5$, and 1.7) up to $\tau = 5$. Thermophoresis governs particle motion driven by temperature gradients; altering this mechanism changes how nanoparticles transport energy through the fluid. In our coupled equations, larger Nt strengthens particle migration driven by thermal gradients and the associated convective/particle–fluid interactions that deliver energy into the fluid phase, producing higher local temperatures. Thus, increasing Nt enhances the transfer of thermal energy via particle motion and raises the temperature profile in the plotted domain.
- Fig. 11 represents the effect of the magnetic parameter H on the temperature distribution. Fig. 11 demonstrates that the temperature distribution increases as the magnetic parameter H increases until $\tau = 5$ for values of magnetic parameter $H = 0.1, 0.6, 1.1$, and 1.6. The temperature distributions increase with increasing magnetic parameter H (the calculations use $H = 0.1, 0.6, 1.1$, and 1.6) up to $\tau = 5$. Two linked effects explain this trend: the imposed magnetic field both damps fluid motion (reducing convective heat removal) and – when Joule or Ohmic heating is included in the energy equation – directly supplies thermal energy via electromagnetic dissipation. The reduced convective cooling, together with any magnetically induced internal heating, raises the fluid temperature, so a stronger magnetic field yields higher temperature values in the boundary layer for the given H values.
- Fig. 12 shows the effect of the Eckert number Ec on the temperature distribution. Fig. 12 demonstrates that the temperature distribution increases as the Eckert number Ec increases until $\tau = 5$ for values of Eckert number $Ec = 0.1, 0.2, 0.3$ and 0.4. Temperature rises when the Eckert number Ec is increased (examined at $Ec = 0.1, 0.2, 0.3$ and 0.4) up to $\tau = 5$. The Eckert number measures the significance of viscous dissipation (conversion of kinetic energy into heat) in the energy balance; higher Ec means viscous friction generates more internal heat. This viscous heating acts as an internal energy source that elevates the temperature within the boundary layer, so an increase in Ec produces higher temperature profiles for the tested values.

The effects of the Lewis number Le, the Brownian motion parameter Nb, the thermophoresis parameter Nt, and the Prandtl number Pr on the concentration are illustrated in Figs. 13–16. Unless otherwise specified in the figure captions, the parameters are set as follows: $M = 0.2$, $n = 0.5$, $\lambda = 0.2$, $H = 0.2$, $R = 0.2$, $\mathrm{Pr} = 2$, $\mathrm{Nt} = 0.5$, $\mathrm{Nb} = 0.5$, $\mathrm{Ec} = 0.1$, $\mathrm{Le} = 3$, and $\alpha = 0.5$.

- Fig. 13 represents the effect of the Lewis number Le on the concentration distribution. Fig. 13 demonstrates that the concentration distribution decreases as the Lewis number Le increases until $\tau = 5$ for values of the Lewis number $Le = 1.8, 2.2, 2.6$, and 3.0. The concentration distribution decreases as the Lewis number Le increases (results given for $Le = 1.8, 2.2, 2.6$, and 3.0) up to $\tau = 5$. Because Le is the ratio of thermal diffusivity to mass diffusivity, larger Le corresponds to smaller species (mass) diffusivity relative to heat diffusion; this produces a thinner concentration boundary layer and reduces the concentration magnitude away from the wall. Therefore, raising Le diminishes mass transport into the fluid domain and lowers the computed concentration profile in the region considered.
- Fig. 14 represents the effect of the Brownian motion parameter Nb on the concentration distribution. Fig. 14 demonstrates that the concentration distribution decreases as the Brownian motion parameter Nb increases until $\tau = 5$ for values of Brownian motion parameter $Nb = 0.4, 0.6, 0.8$, and 1.0. The concentration profile falls when the Brownian motion parameter Nb increases (tested at $Nb = 0.4, 0.6, 0.8$, and 1.0) up to $\tau = 5$. In the concentration equation, Nb appears as a coefficient multiplying Brownian-diffusion terms; larger Nb enhances nanoparticles diffusion away from regions of high concentration, which tends to smooth and reduce the local concentration near the wall. Put differently, stronger Brownian diffusion increases mass transport from the surface into the bulk, lowering the concentration magnitude in the boundary layer for the chosen parameter set.
- Fig. 15 shows the effect of the thermophoresis parameter Nt on the concentration distribution. Fig. 15 demonstrates that the concentration distribution increases as the thermophoresis parameter Nt increases until $\tau = 5$ for values of thermophoresis parameter $Nt = 0.2, 0.4, 0.6$, and 0.8. The concentration increases with larger thermophoresis parameter Nt (shown for $Nt = 0.2, 0.4, 0.6$, and 0.8) up to $\tau = 5$. Thermophoresis drives nanoparticle motion in response to temperature gradients, and in the present coupling, it promotes accumulation patterns that raise the local solute (nanoparticle) concentration within the boundary region. As Nt grows, the thermophoretic flux becomes more significant relative to ordinary diffusion, producing higher concentration values in the plotted domain for the parameter values considered.
- Fig. 16 shows the effect of the Prandtl number Pr on the concentration distribution. Fig. 16 demonstrates that the concentration distribution decreases as the Prandtl number Pr increases until $\tau = 5$ for values of Prandtl number $Pr = 1.2, 1.4, 1.6$, and 1.8. The

concentration distribution decreases when the Prandtl number Pr is increased (examined at $Pr = 1.2, 1.4, 1.6$, and 1.8) up to $\tau = 5$. Although Pr primarily quantifies momentum vs. thermal diffusivity, its change alters the temperature field and thus the thermophoretic and Brownian coupling terms that drive mass transfer; higher Pr sharpens the thermal field (thinner thermal layer), which modifies particle fluxes in a way that reduces solute buildup in the boundary layer. Consequently, increasing Pr indirectly leads to lower concentration magnitudes in the region plotted for the given parameter set.

Figs. 17–20 illustrate the effects of the thermophoresis parameter Nt and the Prandtl number Pr on the Nusselt number, the thermal diffusivity parameter α on the skin friction coefficient, and the Lewis number Le on the Sherwood number, respectively.

- Fig. 17 shows the effect of the thermophoresis parameter Nt on the Nusselt number. Fig. 17 demonstrates that the Nusselt number decreases as the thermophoresis parameter Nt increases until $Nb = 0.22$ for values of thermophoresis parameter $Nt = 0.1, 0.2$, and 0.3.
  The numerical data show that the Nusselt number falls as the thermophoresis parameter Nt is raised (here examined at $Nt = 0.1, 0.2$, and 0.3), the monotonic decrease being observed up to the indicated Brownian-diffusion level $Nb = 0.22$. In the similarity formulation used, Nt appears in the coupled energy-concentration balance through terms that describe particle migration driven by temperature gradients; increasing Nt changes the distribution of nanoparticles and therefore alters the local effective thermal transport near the surface. The practical manifestation in the plots is a reduction of the temperature gradient at the wall, which directly lowers the local Nusselt number because Nu is proportional to that gradient. Mechanistically, stronger thermophoretic forcing tends to drive particles away from the hot region close to the surface, modifying the near-wall microstructure and the effective conduction/convective coupling. When particles migrate under stronger thermophoresis, they can weaken the immediate heat-exchange channel at the wall (either by reducing heat-carrying nanoparticle concentration near the surface or by redistributing energy away from the steepest gradient), hence the heat flux at the surface diminishes and the Nusselt number decreases. Increasing Nt reduces the near-wall temperature gradient via particle migration, so the Nusselt number falls (trend observed up to $Nb = 0.22$).
- Fig. 18 shows the effect of the Prandtl number Pr on the Nusselt number. Fig. 18 demonstrates that the Nusselt number increases as the Prandtl number Pr increases until $R = 0.3$ for values of Prandtl number $Pr = 1.2, 1.5$, and 1.8. The computed curves indicate that the Nusselt number increases with rising Prandtl number Pr for the tested values $Pr = 1.2, 1.5$, and 1.8, and this upward trend persists until the radiation parameter R reaches about 0.30. Physically, Pr measures the ratio of momentum diffusivity to thermal diffusivity; a larger Pr implies relatively minor thermal diffusivity, which confines thermal effects closer to the wall and steepens the temperature gradient there. Since the Nusselt number is directly proportional to the wall temperature gradient, a thinner thermal layer and a larger gradient produce a higher Nu. From an energy–momentum coupling perspective, raising Pr reduces thermal smoothing away from the surface, increasing the local heat removal capacity at the wall (higher conductive flux) until radiative effects become comparable (here quantified by R). At larger R, the added radiative flux alters the balance and can limit the Pr-driven increase; up to R=0.3, however, the dominant effect is the thinner thermal boundary layer produced by higher Pr, so the Nusselt number grows. Larger Pr sharpens the wall temperature gradient and raises Nu (trend valid up to $R \approx 0.3$).
- Fig. 19 shows the effect of the thermal diffusivity parameter α on the skin friction coefficient. Fig. 19 demonstrates that the skin friction coefficient increases as the thermal diffusivity parameter α increases until $M = 1.8$ for values of thermal diffusivity parameter $\alpha = 0.5, 0.7$, and 0.9. The results show that the skin friction coefficient (dimensionless wall shear) increases as the thermal diffusivity α is raised (values compared: $\alpha = 0.5, 0.7$, and 0.9), the trend holding until the fluid parameter M reaches about 1.8. In the coupled problem, α modifies the thermal field, which in turn feeds back into the momentum equation through temperature-dependent source terms or property variations; increased thermal diffusion changes the near-wall thermal structure and thereby alters the velocity gradient at the surface. The observed outcome is a steeper velocity gradient at the wall (higher shear), which produces a larger skin friction coefficient when α increases under the stated parameter set. A plausible physical interpretation is that enhanced heat diffusion alters buoyancy/thermo-viscous coupling and compresses the region over which the velocity adjusts to the surface forcing; even if the far-field velocity is reduced, the near-wall shear can intensify because the flow must transition more abruptly to satisfy the modified thermal–momentum coupling. This yields a larger wall shear stress and hence an increased skin friction coefficient up to the indicated M threshold. Raising α modifies the thermal–momentum coupling so that the near-wall velocity gradient intensifies, increasing skin friction (observed until $M \approx 1.8$).
- Fig. 20 shows the effect of the Lewis number Le on the Sherwood number. Fig. 20 demonstrates that the Sherwood number increases as the Lewis number Le increases until $Pr = 1.7$ for values of thermal diffusivity parameter $Le = 0.2, 0.3$, and 0.4. The Sherwood number grows with increasing Lewis number Le for the tested values $Le = 0.2, 0.3$, and 0.4 a trend that remains valid until the Prandtl number Pr reaches roughly 1.7. Because Le is the ratio of thermal diffusivity to mass diffusivity, a larger Le means smaller mass diffusivity relative to heat diffusion; this produces a thinner concentration boundary layer and steeper concentration gradients at the wall. Since the Sherwood number is proportional to the wall concentration gradient (mass-transfer analogue of the Nusselt number), the enhanced gradient caused by larger Le directly increases the Sherwood number. From the coupling viewpoint, raising Le reduces mass diffusion away from the surface so that concentration differences near the wall are sustained and the mass-flux (per unit driving potential) becomes larger. The interplay with Pr reflects how changes in the thermal field (modified by Pr) feed back into thermophoretic/Brownian fluxes; up to $\mathrm{Pr} \approx 1.7$ the dominant effect is the heightened concentration gradient due to larger Le, and therefore the Sherwood number increases. Increasing Le steepens the wall concentration gradient and raises the Sherwood number (trend holds until $\mathrm{Pr} \approx 1.7$).
- We compared our figures with those presented in the literature and with the graphs produced using *Mathematica*. We found excellent agreement between the results, confirming the accuracy and consistency of our numerical approach.
- A closer examination of the governing equations clarifies how each physical mechanism quantitatively influences the resulting flow and thermal fields. In the momentum equation, the magnetic term acts as a resistive Lorentz force proportional to the magnetic parameter, directly reducing the velocity gradient and thickening the momentum boundary layer. The variable-sheet-thickness function modifies the effective stretching rate, which appears as a nonlinear amplification term, thereby altering shear distribution along the surface. In the energy equation, the Eckert number introduces viscous dissipation through a positive source term proportional to the square of the velocity gradient, while Joule heating contributes an additional electromagnetic heating

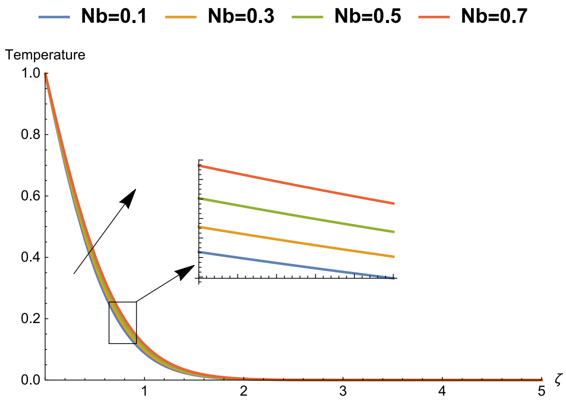

Fig. 9. Influence of the Brownian motion parameter Nb on the temperature.

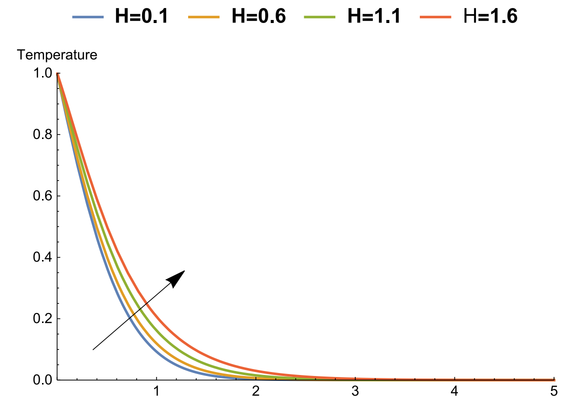

Fig. 11. Influence of the magnetic parameter H on the temperature.

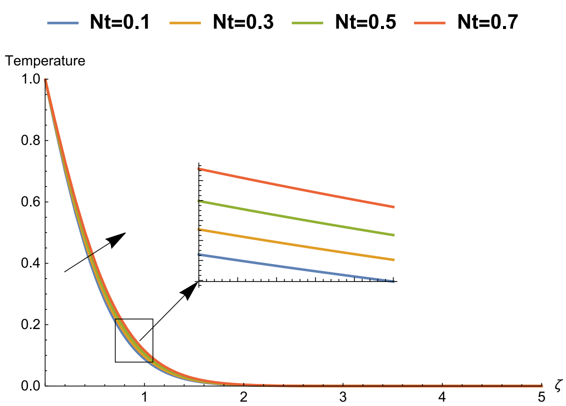

Fig. 10. Influence of the thermophoresis parameter Nt on the temperature.

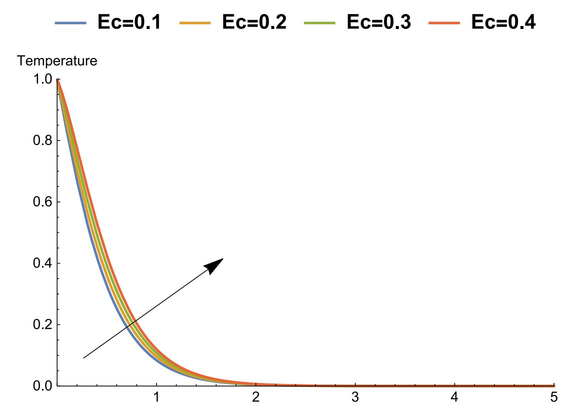

Fig. 12. Influence of the Eckert parameter Ec on the temperature.

term that elevates temperature profiles. Thermal radiation enters as a radiative diffusion term, effectively reducing the temperature gradient and lowering the Nusselt number in high-temperature environments. Brownian motion and thermophoresis appear as coupled diffusion terms in both the energy and concentration equations, where Brownian diffusion enhances thermal dispersion while thermophoresis drives nanoparticles from hot to cold regions, collectively modifying the thermal and concentration boundary layers. These contributions, reflected directly in the dimensionless groups, explain the quantified sensitivity of velocity, temperature, and concentration responses observed in the parametric analysis.

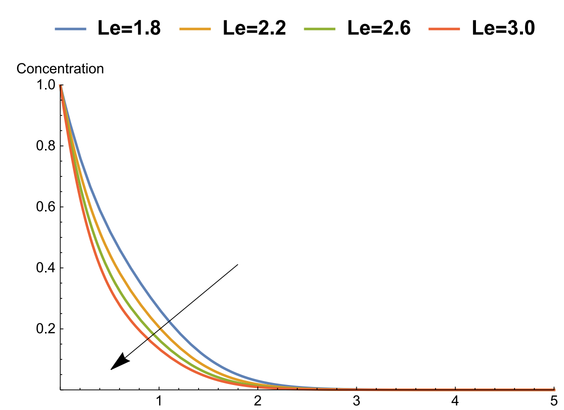

Fig. 13. Influence of the Lewis number Le on the consternation.

7. Conclusion

This study presented a comprehensive analysis of MHD squeezing nanofluid flow with variable sheet thickness, viscous dissipation, Joule heating, thermal radiation, Brownian motion, and thermophoretic transport, solved through an enhanced operational matrix method. The results reveal that the magnetic parameter introduces a Lorentz damping force that suppresses momentum transport while simultaneously increasing thermal energy due to Joule heating. Variable sheet thickness was shown to modulate stretching intensity, thereby altering local strain rates and producing measurable changes in velocity, temperature, and concentration boundary layers. Viscous dissipation and thermal radiation contributed additional internal energy, resulting in significant modification of the Nusselt number in high-shear and high-temperature regimes. The combined effects of Brownian motion and thermophoresis were found to strongly influence nanoparticle redistribution, highlighting their importance in thermal enhancement strategies. Beyond reporting trends, the parametric sensitivity analysis provides meaningful engineering implications. The obtained variations in Nusselt and Sherwood numbers offer guidance on optimizing magnetic field strength, nanoparticle loading, and squeezing rates in practical systems such as MHD-driven microchannel coolers, manufacturing processes involving variable-thickness sheets, and thermally loaded coatings. The accuracy and rapid convergence of the modified operational matrix method confirm its suitability for nonlinear boundary-layer problems, positioning it as a computationally efficient alternative to classical solvers. Future extensions may incorporate temperature-dependent viscosity, nanoparticle agglomeration, or

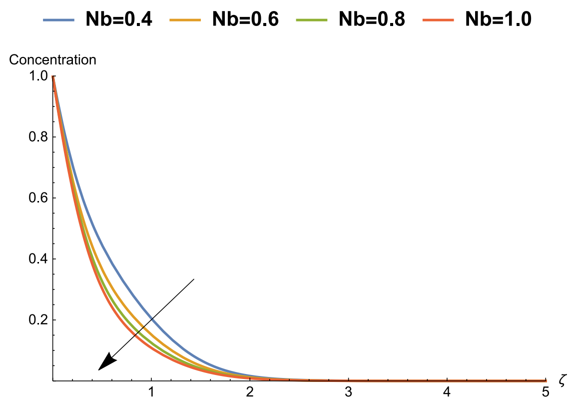

Fig. 14. Influence of the Brownian motion parameter Nb on the consternation.

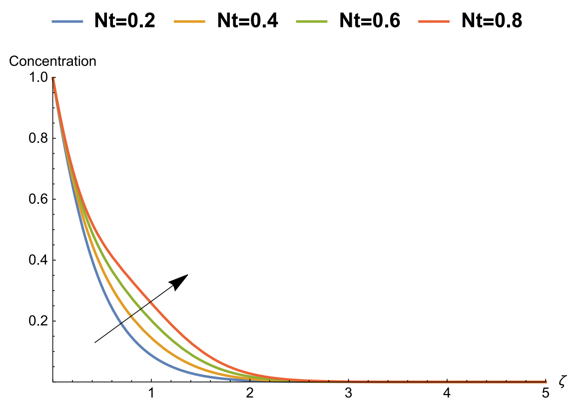

Fig. 15. Influence of the thermophoresis parameter Nt on the consternation.

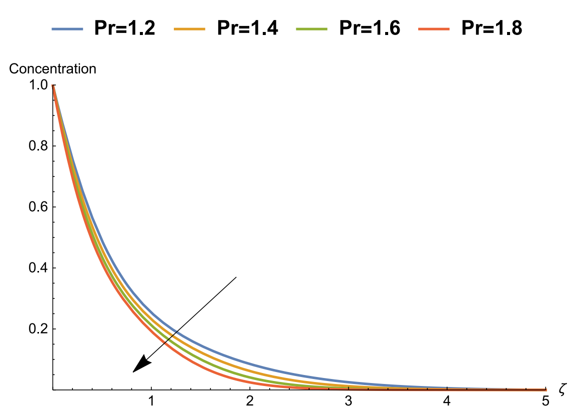

Fig. 16. Influence of the Prandtl parameter Pr on the consternation.

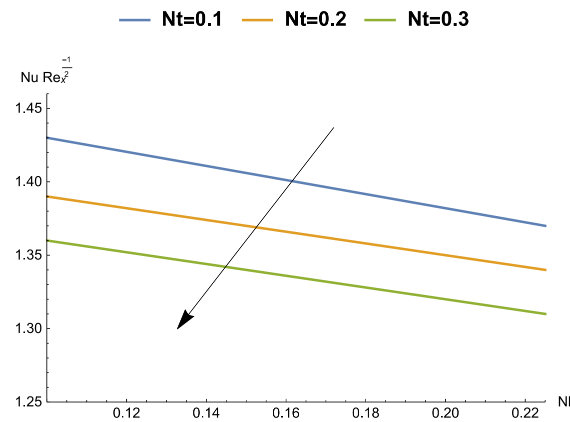

Fig. 17. Influence of the thermophoresis parameter Nt on the Nusselt number.

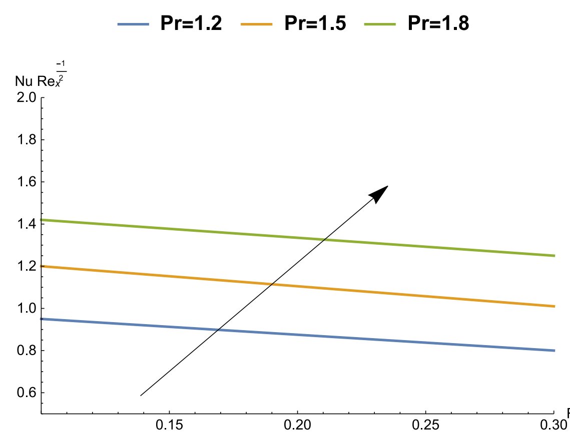

Fig. 18. Influence of the Prandtl parameter Pr on the Nusselt number.

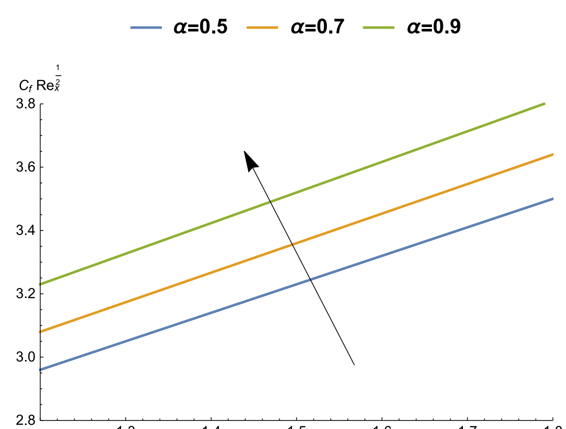

Fig. 19. Influence of the thermal diffusivity parameter α on the skin friction.

transient squeezing dynamics, and can be coupled with experimental validation for specific industrial devices. Overall, the study delivers physically consistent insights into complex thermo-hydrodynamic mechanisms and establishes a solid foundation for engineering design and optimization involving MHD nanofluid systems.

Finally, we will write the physical significance of MHD, Viscous dissipation, and thermal radiation impacts. The application of a magnetic field introduces a Lorentz force into the flow, which acts opposite to the direction of motion and therefore suppresses fluid velocity. In the context of this study, increasing the magnetic parameter reduces the momentum transport and thickens the velocity boundary layer, demonstrating the classical magnetic-braking effect observed in electrically conducting fluids. This mechanism is important because it allows external control over the flow structure and modifies heat transfer behavior through the generation of Joule heating, leading to higher temperatures within the boundary layer. Viscous dissipation represents the conversion of kinetic energy into thermal energy due to frictional forces within the fluid. Its contribution appears in the energy equation through the Eckert number, which quantifies the relative importance of viscous heating. In this study, increasing viscous dissipation enhances the thermal energy in the boundary layer, resulting in higher temperature distributions and a thicker thermal layer. This effect is particularly significant in high-speed flows, strong stretching environments, and in

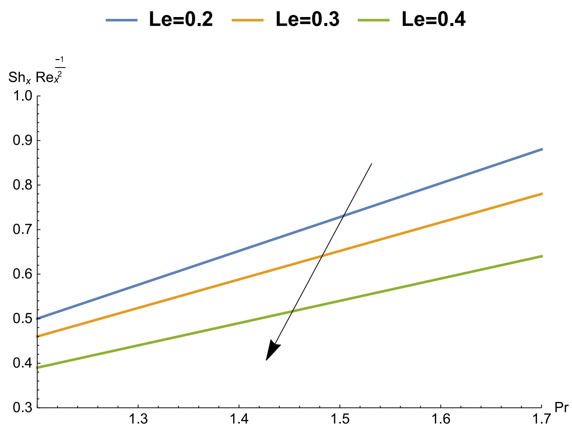

Fig. 20. Influence of the Lewis number Le on the Sherwood number.

applications where fluid friction is non-negligible, such as lubrication, polymer extrusion, and geothermal processes. Thermal radiation introduces an additional mode of heat transfer that becomes prominent in systems involving high temperatures or radiatively active fluids. Through the radiation parameter, the radiative heat flux effectively increases the thermal conductivity of the nanofluid, allowing more heat to penetrate the boundary layer. In this manuscript, higher thermal radiation levels lead to elevated temperature distributions and reduced temperature gradients near the wall, which in turn alter the heat transfer rate. This mechanism is relevant in applications such as solar collectors, thermal processing, combustion chambers, and advanced energy systems where radiative effects play a dominant role.

CRediT authorship contribution statement

Mahmmoud M. Syam: Writing – review & editing, Methodology, Formal analysis. **Muhammed I. Syam:** Software, Investigation. **Kenan Yildirim:** Software.

Declaration of competing interest

The authors declare that they have no known competing financial interests or personal relationships that could have appeared to influence the work reported in this paper.

Data availability

No data was used for the research described in the article.

References

[1] T. Hayat, M.I. Khan, M. Waqas, A. Alsaedi, On Cattaneo-Christov heat flux in the flow of variable thermal conductivity Eyring–Powell fluid, Results Phys. 7 (2017) 50–446.

[2] M. Jalil, S. Asghar, S.M. Imran, Self-similar solutions for the flow and heat transfer of Powell-Eyring fluid over a moving surface in a parallel free stream, Int. J. Heat Mass Transfer 65 (2013) 9–73.

[3] N.S. Akbar, A. Ebaid, Z.H. Khan, Numerical analysis of magnetic field effects on Eyring-Powell fluid flow towards a stretching sheet, J. Magn. Magn. Mater. 382 (2015) 8–355.

[4] T. Syam, M.M. Syam, A. Khan, M.I. Syam, Statistical analysis of car data using analysis of covariance (ANCOVA), in: Mathematical Methods for Engineering Applications, ICMASE 2022, in: Springer Proc Math S.

[5] A. Rehman, S. Achakzai, S. Nadeem, Iqbal S., Stagnation point flow of Eyring Powell fluid in a vertical cylinder with heat transfer, J. Power Technol. 96 (2016) 57–62.

[6] Syam, M. Mahmmoud, et al., Computational study of magnetohydrodynamic squeeze flow between infinite parallel disks, Int. J. Thermofluids (ISSN: 2666-2027) 24 (2024) 100847.

[7] I. Khan, K.U. Rehman, M.Y. Malik, Physical aspects of nanoparticles in non-Newtonian liquid in the presence of chemically reactive species through parabolic approach, Results Phys. 7 (2017) 9–2540.

[8] Choi SUS, Enhancing thermal conductivity of fluids with nanoparticles, in: ASME International Mechanical Engineering Congress and Exposition, New York, 1995, pp. 99–105.

[9] Syam, M. Mahmmoud, et al., Investigation of slip flow dynamics involving Al_2O_3 and Fe_3O_4 nanoparticles within a horizontal channel embedded with porous media, Int. J. Thermofluids 24 (2024) 100934.

[10] H.U. Kang, S.H. Kim, J.M. Oh, Estimation of thermal conductivity of nanofluids for the application of heat transfer fluids, Exp. Heat Transf. 19 (2006) 91–181.

[11] Syam, M. Mahmmoud, et al., Impacts of energy transmission properties on non-Newtonian fluid flow in stratified and non-stratified conditions, Int. J. Thermofluids (ISSN: 2666-2027) 23 (2024) 100824.

[12] B. Mahanthesh, B.J. Gireesha, R.S.R. Gorla, Unsteady three-dimensional MHD flow of a nano Eyring-Powell fluid past a convectively heated stretching sheet in the presence of thermal radiation, viscous dissipation and Joule heating, J. Assoc. Arab. Univ. Basic Appl. Sci. 23 (2017) 75–84.

[13] W. Ibrahim, Nonlinear radiative heat transfer in magnetohydrodynamic (MHD) stagnation point flow of nanofluid past a stretching sheet with convective boundary condition, Propuls. Power Res. 4 (2015) 9–230.

[14] Z. Abbas, R. Perveen, M. Sheikh, I. Pop, Thermophoretic diffusion and nonlinear radiative heat transfer due to a contracting cylinder in a nanofluid with generalized slip condition, Results Phys. 6 (2016) 7–1080.

[15] Syam, M. Mahmmoud, et al., Thermal and hydrodynamic analysis of MHD nanofluid flow over a permeable stretching surface in porous media: Comparative study of Fe3o4, Cu, and Ag nanofluids, Int. J. Thermofluids (ISSN: 2666-2027) 26 (2025) 101055, http://dx.doi.org/10.1016/j.ijft.2025.101055.

[16] S. Nadeem, S. Saleem, Mixed convection flow of Eyring–Powell fluid along a rotating cone, Results Phys. 4 (2014) 54–62.

[17] M.Y. Malik, A. Hussain, S. Nadeem, Boundary layer flow of an Eyring–Powell model fluid due to a stretching cylinder with variable viscosity, Sci. Iran. 20 (2013) 21–313.

[18] A.M. Rashad, A.J. Chamkha, M. Modather, Mixed convection boundary-layer flow past a horizontal circular cylinder embedded in a porous medium filled with a nanofluid under convective boundary condition, Comput. & Fluids 86 (2013) 8–380.

[19] Syam, M. Mahmmoud, et al., Heat transfer characteristics of graphene oxide nanofluid in unsteady squeezing flow between plates, Int. J. Thermofluids (ISSN: 2666-2027) 30 (2025) 101448, http://dx.doi.org/10.1016/j.ijft.2025.101448.

[20] A. Shojaei, A.J. Amiri, S.S. Ardahaie, K. Hosseinzadeh, D.D. Ganji, Hydrothermal analysis of Non-Newtonian second grade fluid flow on radiative stretching cylinder with Soret and Dufour effects, Case Stud. Therm. Eng. 13 (2019) 100384.

[21] K.U. Rehman, M.Y. Malik, O.D. Makinde, Parabolic curve fitting study subject to Joule heating in MHD thermally stratified mixed convection stagnation point flow of Eyring-Powell fluid induced by an inclined cylindrical surface, J. King Saud Univ.-Sci. (2018) http://dx.doi.org/10.1016/j.jksus.2017.02.003.

[22] Syam, M. Mahmmoud, et al., Exploring boundary layer flow dynamics on a semi-infinite plate: A numerical study of transpiration effects and dual solutions, Nonlinear Dyn. Syst. Theory (ISSN: 1562-8353) 25 (4) (2025).

[23] D.H. Babu, P.V. Satya Narayana, Joule heating effects on MHD mixed convection of a Jeffrey fluid over a stretching sheet with power law heat flux: a numerical study, J. Magn. Magn. Mater. 412 (2016) 93–185.

[24] A. Kamran, S. Hussain, M. Sagheer, N. Akmal, A numerical study of magnetohydrodynamics flow in casson nanofluid combined with joule heating and slip boundary conditions, Results Phys. 7 (2017) 3037–3048.

[25] H. Sajjadi, A.A. Delouei, M. Sheikholeslami, M. Atashafrooz, S. Succi, Simulation of three dimensional MHD natural convection using double MRT Lattice Boltzmann method, Phys. A Stat. Mech. Appl. 515 (2019) 474–496.

[26] Syam, M. Mahmmoud, et al., Nonlinear dynamics of laminar flow in porous channels: Effects of wall dilation and inertial–viscous interplay, Int. J. Thermofluids (ISSN: 2666-2027) 27 (2025) 101259, http://dx.doi.org/10.1016/j.ijft.2025.101259.

[27] A.V. Kuznetsov, The onset of nanofluid bioconvection in a suspension containing both nanoparticles and gyrotactic microorganisms, Int Commun. Heat Mass Transf. 37 (10) (2010) 1421–1425.

[28] A.V. Kuznetsov, Nanofluid bioconvection in water-based suspensions containing nanoparticles and oxytactic microorganisms: oscillatory instability, Nanoscale Res. Lett. 6 (1) (2011) 100.

[29] Syam, M. Mahmmoud, Thermal and fluid behavior of nanofluids over a rotating disk: Influence of Darcy–Forchheimer and slip conditions, Int. J. Thermofluids (ISSN: 2666-2027) 28 (2025) 101316, http://dx.doi.org/10.1016/j.ijft.2025.101316.

[30] S.M. Syam, M. Zain, R. Alshateri, A. Al-Dulaimi, M.I. Syam, A modified operational matrix method for investigation of the nonlinear dynamics of fractional systems, Fractals 33 (8) (2025) 2540155, http://dx.doi.org/10.1142/S0218348X25401553.

[31] M.I. Syam, H. Alahbabi, R. Alomari, S.M. Syam, S.M. Hussein, S. Rabih, N. Al Saafeen, A numerical study for fractional problems with nonlinear phenomena in physics, Prog. Fract. Differ. Appl. 10 (3) (2024) 451–461, http://dx.doi.org/10.18576/pfda/100310.

[32] S.H. Altoum, M.I. Syam, S.M. Syam, H.A.Z. Al-Bonsrulah, A.M. Hussin, Efficacy of magnetic force on nanofluid laminar transportation and convective flow, J. Magn. Magn. Mater. 581 (2023) 170964, http://dx.doi.org/10.1016/j.jmmm.2023.170964.

[33] M.M. Nandeppanavar, M.N. Siddalingappa, Effect of viscous dissipation and thermal radiation on heat transfer over a non-linearly stretching sheet through a porous medium, Int. J. Appl. Mech. Eng. 18 (2) (2013) 461–474, http://dx.doi.org/10.2478/ijame-2013-0027.

[34] M.M. Nandeppanavar, M.C. Kemparaju, S. Shakunthala, MHD stagnation point slip flow due to a non-linearly moving surface with effect of non-uniform heat source, Nonlinear Eng. 8 (1) (2019) 270–282, http://dx.doi.org/10.1515/nleng-2017-0109.

[35] Z. Abdelmalek, I. Khan, M.W.A. Khan, K.U. Rehman, E.-S. M. Sherif, Computational analysis of nano-fluid due to a non-linear variable thicked stretching sheet subjected to Joule heating and thermal radiation, J. Mater. Res. Technol. 9 (5) (2020) 11035–11044, http://dx.doi.org/10.1016/j.jmrt.2020.07.085.

[36] S. Mukhtar, S. Rana, M. Mansoor, T. Arooj, Q.M. Ul Hassan, R. Shah, MHD viscoelastic nanofluid flow across an extended plate using mixed convection and thermal radiation, Front. Energy Res. 12 (2024).

[37] M.S. Sankari, M. Eswara Rao, F. Awwad, E.A.A. Ismail, O.D. Makinde, W. Khan, Influence of dual stratification on the magnetohydrodynamic flow of Jeffrey nanofluid over an exponentially stretching permeable sheet with viscous dissipation and Joule heating, Front. Chem. (2025).

[38] J. Mathews, H. Talla, Unsteady magnetohydrodynamic free convection flow of Al_2O_3Cuwater nanofluid over a permeable linear stretching sheet through a porous medium with viscous dissipation and heat source/sink, J. Therm. Eng. 11 (2) (2025) 344–356.

[39] M.M. Magdy, W. Abbas, K.S. Mekheimer, et al., Ferro-fluid flow and heat transfer over unsteady stretching sheet in the presence of a nonuniform magnetic field, J. Nonlinear Math. Phys. (2025).

[40] V. Adilakshmi, A. Akgül, G. Venkata Ramana Reddy, et al., Thermal radiation and diffusion effects on MHD Sisko fluid flow over a nonlinearly stretchable porous sheet, Bound. Value Probl. (2025).

[41] K.O. Ogboru, M.M. Lawal, A.M. Okedoye, Dissipative non-slip MHD nanofluid flow with variable viscosity and thermal conductivity in the presence of arrhenius chemical reaction, Eur. J. Theor. Appl. Sci. 2 (3) (2024) 592–608.

[42] Khadija Rafique, Zafar Mahmood, Numerical investigation of entropy generation of joule heating in non-axisymmetric flow of hybrid nanofluid towards stretching surface, J. Comput. Des. Eng. 11 (2) (2024).

[43] S. Sharma, S. Jain, Convective heat transfer flow of MHD hybrid nanofluid over a stretching sheet with velocity and thermal slip, Int. J. Math. Phys. 15 (2) (2024).